

AD-A242 748



Final Technical Report



DAMAGE MECHANISMS IN COMPOSITES

submitted to

Dr. Steven G. Fishman
Program Manager, Non-Metallic Materials
Office of Naval Research, Code 1131
800 North Quincy Street
Arlington, VA 22217

ONR Contract Number N00014-86-K-0125

August, 1991

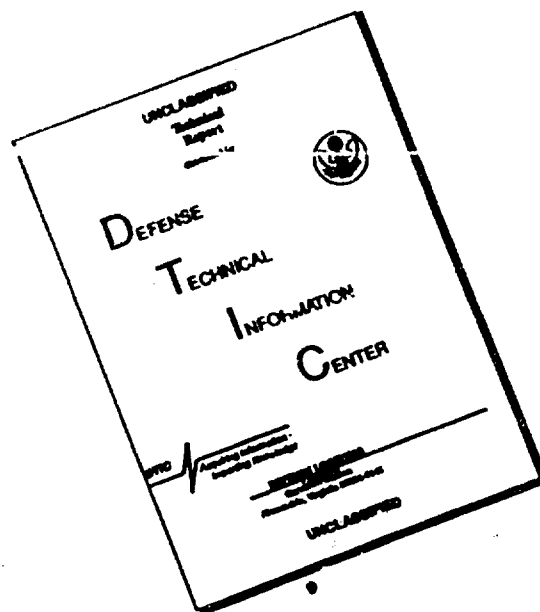
DISTRIBUTION STATEMENT A

Approved for public release;
Distribution Unlimited

Submitted by: Steven Nutt
Division of Engineering
Brown University
Providence, RI 02912
(401) 863-2862

91-15434

DISCLAIMER NOTICE



THIS DOCUMENT IS BEST
QUALITY AVAILABLE. THE COPY
FURNISHED TO DTIC CONTAINED
A SIGNIFICANT NUMBER OF
PAGES WHICH DO NOT
REPRODUCE LEGIBLY.

EXECUTIVE SUMMARY

Mechanically induced residual stresses are an inherent feature of permanently deformed metal-matrix composites such as Al-SiC. The presence of hard SiC reinforcements promotes non-homogeneous flow in the matrix, resulting in residual stresses when the applied loads are removed. These residual stresses are potentially important because of the effect on cavitation and other damage mechanisms leading to composite failure. We have attempted to simulate the residual stresses in the composite by solving appropriate boundary value problems using the finite element method. Using this approach, we have compared predicted average residual elastic strains with those measured by neutron diffraction for Al-SiC composites subjected to different loading histories. The composite studied was a 2009 aluminum alloy reinforced with 15 vol % SiC whiskers. Samples were subjected to various levels of plastic strain and unloaded before measuring peak shifts in neutron diffraction patterns to determine residual strains. Residual strains were also calculated using a unit cell model and a modified Eshelby method. The Eshelby method predicted a linear dependence of residual elastic strains on the imposed deformation, in disagreement with experimental results. However, the finite element calculations produced good quantitative agreement with experimental measurements and indicated that inclusion geometry can significantly affect the values of even average field quantities. Interestingly, the thermally induced residual strains (from quenching) were quickly dominated by the mechanically induced residual strains, even for relatively small amounts of composite plastic deformation. The excellent agreement between predicted and measured residual strains suggest that it is possible to predict microstructural-level stresses with unit cell, continuum-based models using the finite element method. Future work will address residual stresses in particulate composites and the effects of more complex loading paths.

We have also been engaged in studies of environmental effects on creep damage mechanisms in ceramic matrix composites. The benefits of whisker reinforcement of monolithic ceramics with regard to fracture toughness is well-established, and because of the inherent thermal and chemical stability, it is important to determine to what extent these benefits extend to high-temperature mechanical properties. Samples of SiC whisker-reinforced alumina were deformed under constant load at 1200-1400°C in compression. Parallel experiments were conducted in air and in inert atmosphere in order to isolate the effects of test ambient. Although the stress dependence of the strain rate was independent of test ambient, the strain rates in the aerobic ambient were 2-5 times greater. Microscopic observations of crept samples revealed that glass phase

accumulated at grain boundary-interface junctions and facilitated cavitation, despite the macroscopic state of uniaxial compression. The glass phase was generated primarily by thermal oxidation of SiC exposed at the specimen surface, which subsequently penetrated the composite along internal boundaries. Susceptibility to oxidation is likely to pose a problem for any carbide reinforced ceramic, especially for tensile loadings, unless the reaction can be controlled through appropriate protective coatings.

Presently, we are investigating the effects of whisker volume fraction on creep response, and comparing the creep response in compression versus flexure using an inert test ambient. Preliminary results indicate that the decrement associated with adding a given vol% of SiC reinforcement *decreases* as the volume fraction increases, and that there is little improvement in strain rate for volume fractions greater than ~ 30%. However, it is not clear why this is so, or how the aspect ratio of the fibers might affect the observed dependence. Experiments and calculations are presently in progress to investigate these issues.

Also included in this report is publications describing the microstructural evolution and micromechanical modeling of deformation in 2124 Al-SiC_w composites.

This paper is the result of collaborative research involving several members of the engineering faculty at Brown. In this material, the yield strength was relatively insensitive to aging time despite a substantial change in the yield strength of the control alloy. FEM calculations predicted the qualitative trends observed, although the complexity of the microstructure requires greater understanding than is currently available. Microstructural observations of damage mechanisms occurring during tensile deformation at 20°C and 300°C indicated that cavitation at fiber ends was important at both temperatures. Cavitation was localized near the fracture surface at room temperature, but occurred through the gage length at high temperatures, suggesting that cavitation may play an important role during creep rupture of these and similar composites. This issue will be the subject of investigation in the coming year.

Statement A per telecon
Dr. Steven Fishman ONR/Code 1131
Arlington, VA 22217-5000

NWW 11/21/91



Accession For
N1131 000001
Spec Tab
Inventory
Justification

By
Distribution

Classified by
Exempt from

A-1

Reprinted from the Journal of the American Ceramic Society, Vol. 74, No. 6, June 1991
Copyright © 1991 by The American Ceramic Society, Inc.

Atmospheric Effects on Compressive Creep of SiC-Whisker-Reinforced Alumina

Pete Lipetzky and Steven R. Nutt

Atmospheric Effects on Compressive Creep of SiC-Whisker-Reinforced Alumina

Pete Lipetzky and Steven R. Nutt*

Division of Engineering, Brown University, Providence, Rhode Island 02912

David A. Koester* and Robert F. Davis*

Department of Materials Science and Engineering, North Carolina State University,
Raleigh, North Carolina 27695-7907

A SiC-whisker-reinforced alumina composite was crept in compression at 1200° to 1400°C in an air ambient and in nitrogen. The data were described by a power-law-type constitutive relation. The measured value of the stress exponent was $n = 1$ at 1200°C and $n = 3$ at 1300° and 1400°C in both ambients. TEM observations were correlated with the measured creep response to determine active deformation mechanisms. Values of $n = 1$ were associated with diffusional creep and unaccommodated grain-boundary sliding, while values of $n = 3$ were associated with increased microstructural damage in the form of cavities. Experiments conducted in circulated air resulted in higher creep rates than comparable experiments in nitrogen. The accelerated creep rates were caused by the thermal oxidation of SiC and the resultant formation of a vitreous phase along composite interfaces. The glassy phase facilitated cavitation, weakened interfaces, and enhanced boundary diffusion. [Key words: creep, alumina, composites, silicon carbide, oxidation.]

I. Introduction

THE development of whisker-reinforced ceramic composites has created new applications for ceramics because of improvements in fracture toughness and increased resistance to thermal shock, erosion, and creep when compared to monolithic materials.¹ For example, alumina reinforced with SiC whiskers is presently used for cutting tool inserts, valves, pump components, and extrusion dies. In addition, whisker-reinforced composites of silicon nitride, mullite, and molybdenum disilicide have shown similar improvements in mechanical properties and have potential for use in a variety of structural applications.²⁻⁶

Because of the inherent thermal and chemical stability of ceramics and the benefits of whisker reinforcement, it is natural to consider the mechanical behavior of ceramic composites at high temperatures. Use of ceramic materials in high-temperature structural applications is often limited by poor creep resistance. However, several recent studies have shown that whisker reinforcement can lead to marked improvements in creep resistance.⁷⁻¹² Under creep conditions, the mechanical response of ceramic composites is strongly affected by the presence of the reinforcing phase, the strength of the interfacial bond between the fiber and the matrix, and the chemical stability of the interface. Oxidation reactions

which occur during creep can degrade the interface properties, leading to microstructural damage that strongly affects the creep response.⁸ Thus, before ceramic composites can be reliably used in structural applications at high temperatures, it is necessary to understand the effect of test ambients on the mechanisms of damage and deformation that occur during creep. The objective of the present study is to determine the effects of temperature, stress, and test ambient on the compressive creep response of a whisker-reinforced ceramic composite and to correlate these findings with transmission electron microscope (TEM) observations of crept samples in order to determine mechanisms of deformation and damage.

A widely studied ceramic composite used in cutting tool applications consists of an alumina matrix reinforced with SiC whiskers.^{1-3,7-9,11} The composites are typically fabricated by hot-pressing high-purity alumina powder blended with SiC whiskers in volume fractions ranging from 0.15 to 0.35. Whiskers typically have aspect ratios of 5 to 10 and tend to lie perpendicular to the hot-pressing axis (HPA). The composite microstructure is almost completely free of residual glass phase,⁶ and in this sense constitutes a model material for studies of composite creep behavior. (Ceramic systems such as silicon nitride often require additives for densification, and these additives generally remain in the composite as residual glass phase.) Most studies of composite creep to date have been performed in bending under a constant applied load, and it has been shown that the creep resistance of the composites is generally far superior to the unreinforced matrices.⁷⁻¹² In two of these studies, creep experiments were performed at 1400° to 1600°C in air, and microstructural observations suggested that the composites deformed by dislocation glide.^{7,12} However, similar creep tests at lower temperatures (1200° to 1400°C) showed that the dominant deformation mechanism was grain-boundary (and interface) sliding resulting from diffusion, and that the sliding was often unaccommodated, causing cavitation at grain-boundary-interface junctions.^{8,13} All of the studies mentioned above were conducted in air ambients. Under these conditions, a thermal oxidation reaction is known to occur in which the SiC whiskers exposed at the surface are oxidized.¹⁴⁻¹⁶ The effect of test ambient on creep response is thus an important issue. A recent study showed that test ambients of argon and air had a small but irreversible effect on the compressive creep rates of similar composites.¹¹ The research described in the following sections attempts to further explore these effects and to identify active mechanisms of deformation and damage.

II. Experimental Procedure

The composite material selected for the current investigation was a SiC-whisker-reinforced alumina.* Microstructural

J. L. Routbort—contributing editor

Manuscript No. 197300 Received September 11, 1990; approved February 12, 1991.

Work at Brown University supported by the Office of Naval Research through Contract No. N00014-86-K-0125

*Member, American Ceramic Society

*WG-300, Greenleaf Corp., Saegertown, PA

characterization of the as-fabricated composite showed an average grain size of 1 to 2 μm and a reinforcement volume fraction of 0.33. Additional microstructural details have been described previously.⁸ The primary processing defects in the as-fabricated composite material consisted of occasional whisker-free channels of matrix.⁸ The observed structure was attributed to a granulation process often used to produce controlled agglomerates of the constituents prior to hot-pressing.¹⁷

Compressive creep experiments were conducted in an apparatus designed to apply constant stress in a regulated ambient of continuously circulated dry nitrogen or circulated air.¹⁸ Cylindrical specimens 4 mm in diameter and 8 mm in length were ground and polished prior to testing. Creep experiments were conducted at 1200° to 1400°C under applied stresses of 25 to 250 MPa. Samples were held at conditions of constant stress and temperature until a constant creep rate was observed for a least 10 h. Plots of strain rate versus time were used to determine that a constant creep rate had been reached and maintained. The stress (or temperature) was then increased incrementally, and the procedure was repeated. An optical pyrometer sighted on the silicon carbide platen adjacent to the specimen was used to control the furnace temperature. When the pyrometer registered the desired test temperature, the load was applied and the experiment commenced. The test temperature was then maintained to within 1°C of the preset value. Upon completion of a test, samples were cooled rapidly under constant stress in an effort to retain the deformed microstructure. The maximum strain allowed in each specimen was 3%, thus minimizing nonuniform specimen deformation ("barrelling").

The microstructures of as-fabricated and crept specimens were characterized by TEM. Thin foils were prepared by sectioning a disk from the center of each cylindrical specimen. Disks were ground, polished, and dimple-polished prior to ion milling. Thinned specimens were examined in an analytical electron microscope operated at 120 kV and equipped with an energy dispersive X-ray spectrometer (EDS). TEM observations of the as-received composite revealed a microstructure that was virtually free of residual glass phase. Accumulations of glass at triple grain junctions and at grain-boundary-interface junctions were rarely observed. Figure 1(A) is an image of a typical grain-boundary-interface junction in the as-fabricated composite. No intragranular pores or grain-boundary cavities were observed in the composite, indicating that densification was virtually 100%. Close examination of the SiC-Al₂O₃ interface using high-resolution methods revealed a thin

layer (1 nm thick) of noncrystalline material (Fig. 1(B)). The interface film was presumed to be SiO₂, a native oxide commonly present on SiC. However, the matrix grain boundaries were ostensibly glass-free, within the resolution of the dark-field and high-resolution imaging techniques used (~1 nm).

III. Results

(I) Creep Experiments

(A) *Inert Ambient:* A series of experiments at constant temperature and incrementally increased stress was performed to determine the steady-state creep rates of the composite over a wide range of conditions. The steady-state strain rate was ascertained from plots of strain rate versus time, as shown in Fig. 2. After an initial transient, steady-state creep was typically established, and the associated strain rate was determined. Creep rates determined for a range of stress/temperature conditions are summarized in Fig. 3, a log-log plot of the measured secondary creep rates versus applied stress for creep experiments performed in nitrogen and in air. The data conform to a power-law-type constitutive relation in which the creep rate is proportional to the applied stress raised to an exponent, n (given by the slope of the lines in Fig. 3). The value of the stress exponent for creep at 1200°C in nitrogen was approximately 1, while at 1300°C, the stress exponent was approximately 3.5. The data for tests at 1400°C appear bilinear, with stress exponents of $n = 1$ at low stresses and $n = 3.5$ at higher stresses, a phenomenon generally attributed to a stress-activated change in deformation mechanism. Density measurements were performed on selected specimens before and after creep experiments to determine the cavitation component of creep strain. At 1200°C, cavitation accounted for about 10% of the creep strain, while at 1300°C, the cavitation component of creep strain was about 30%. The total creep strain in each specimen was different, however (0.009 at 1200°C and 0.015 at 1300°C).

(B) *Oxidizing Ambient:* A series of similar creep experiments were conducted in air, the results of which are summarized in Fig. 3. As in the experiments performed in nitrogen, the data conformed to a power-law constitutive relation. The stress exponents over the entire range of applied stresses were $n = 3.3$ for 1300°C and $n = 3.5$ for 1400°C. There was no indication of a bilinear response at either temperature.

A comparison of creep data acquired in nitrogen and in air showed that, although the stress exponents were similar, the strain rates were significantly higher for tests conducted in the

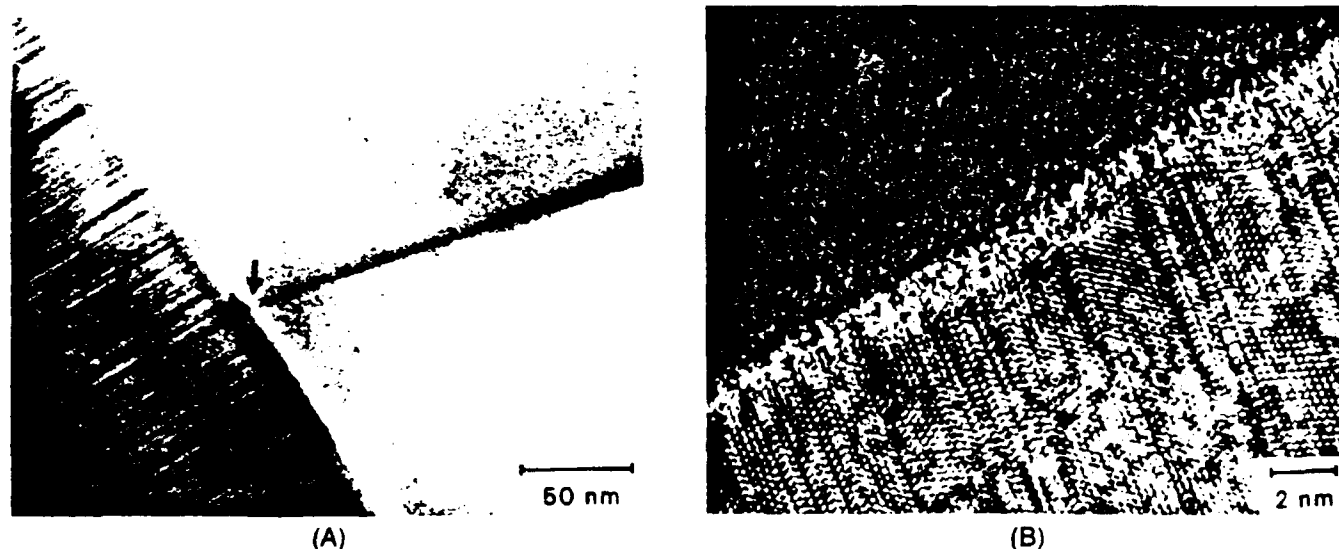


Fig. 1. Characteristics of as-fabricated composite microstructure: (A) a typical grain-boundary interface (GBI) junction, showing an absence of glass phase (arrow); (B) a high-resolution TEM image of interface between SiC whisker and Al₂O₃ matrix showing a thin layer of amorphous silica (arrow).

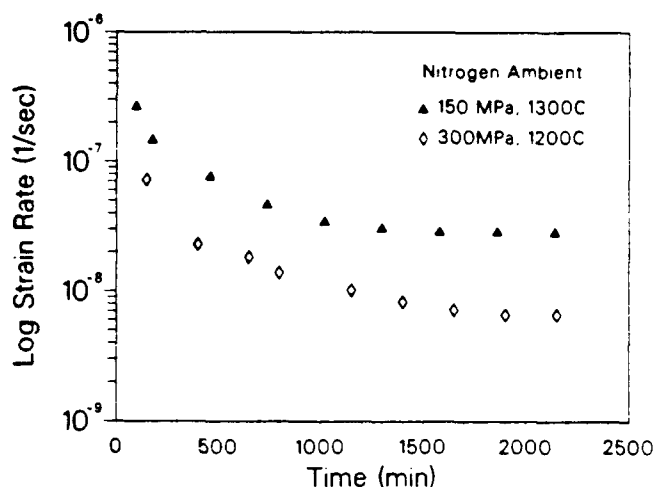


Fig. 2. Strain rate versus time curves for Al_2O_3 -SiC composites subjected to different stress levels at 1200° and 1300°C in nitrogen.

oxidizing ambient (Fig. 3). The strain rates increased by factors of 3 for tests performed at 1300°C, while specimens tested at 1400°C in air showed a fivefold increase in strain rate compared to those crept in nitrogen. At stresses below 50 MPa, the effect of test ambient on creep response diminished, and at a stress level of 25 MPa there was no appreciable effect on strain rate. Specimens creep-tested in air at both temperatures were discolored (from green to gray) as a result of an oxidation reaction during testing. However, specimens tested in nitrogen showed no color change.

Activation energies for secondary creep in air and in nitrogen were obtained from Arrhenius plots (Fig. 4). At low temperature, creep experiments in air and in nitrogen yielded activation energies of 270 and 210 kJ/mol, respectively, while at higher temperatures, the activation energies were 650 and 970 kJ/mol, respectively. The marked change in activation energy occurred at about 1280°C.

It has been demonstrated that creep mechanisms can be inferred from the measured value of the stress exponent for pure metals and monolithic ceramics.^{19,20} Stress exponents of 3 in crept monolithic ceramics have been attributed to dislocation climb from Bardeen-Herring sources, while stress exponents of 1 have been attributed to diffusional creep.²¹ However, for composites and most multiphase ceramics, deformation mechanisms cannot be reliably deduced from creep data alone because of complex interactions between microstructural constituents that make model representations intractable. For

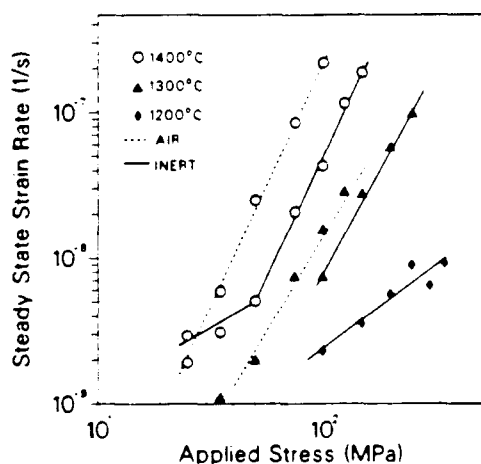


Fig. 3. Steady-state strain rates versus applied stress for creep experiments performed in nitrogen and in air at 1200° to 1400°C. The data conform to power-law-type constitutive relations.

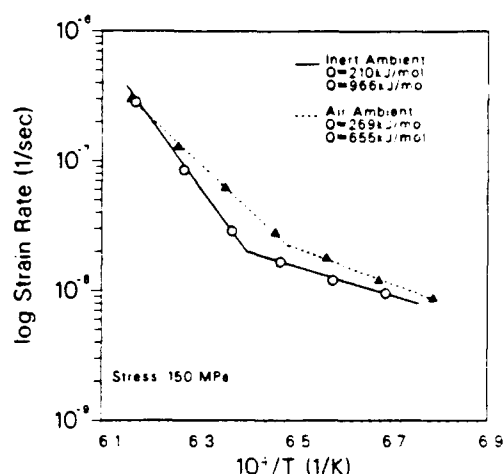


Fig. 4. Arrhenius plots showing increase in activation energy for creep at a threshold temperature of ~1280°C.

this reason, deformation mechanisms in composites were determined by comparing measured creep response with direct observations of the deformed microstructures using TEM.

(2) TEM Observations

(A) *Inert Ambient:* The microstructures of samples crept at 1200°C in nitrogen (which yielded a stress exponent of 1), were examined by TEM. The creep damage was slight but detectable. One of the features characteristic of these microstructures was the formation of small (0.05 to 0.1 μm) voids at a small percentage of the observable grain-boundary-interface (GBI) junctions (Fig. 5(A)). A thin glassy film was sometimes observed lining the interior of these voids, which were observed only after creep, and compositional analysis by EDS showed that the phase contained primarily silicon and aluminum, as well as small concentrations of sulfur and molybdenum (Fig. 5(B)). A second microstructural feature that resulted from creep at 1200°C was the development of corrugated or faceted alumina grain boundaries (Fig. 5(C)). Grain-boundary facets in alumina are often associated with boundary migration during creep.²¹ The energy of certain grain boundaries can be lowered by the development of facets, provided the resulting facet planes have sufficiently low energy to offset the increase in boundary area. Facets on both low-angle and high-angle grain boundaries were observed, and the facets were not detected in the material prior to deformation. The facets ranged in height from 0.05 to 0.2 μm with a mean height of approximately 0.1 μm , while the step spacing varied from 0.05 to 0.8 μm . Grain-boundary faceting was observed approximately half as often as GBI cavities.

The microstructures of samples creep-tested at 1300° and 1400°C in nitrogen were also examined by TEM. The samples were characterized by voids at GBI junctions, at whisker-whisker contact areas, and at alumina triple grain junctions, as well as by corrugated grain boundaries. Figure 6 shows a typical cavity approximately 0.1 μm in diameter at a triple grain junction. Cavities at these sites were typically triangular, with small amounts of glassy phase at the corners. The voids at GBI junctions were larger (0.05 to 0.3 μm) and more frequent (5% to 10% of the junctions) than in specimens tested at 1200°C. Also, voids at GBI junctions were approximately twice as frequent as voids at triple grain junctions. Voids in these specimens often had a thin lining of glassy phase, as shown in Fig. 6, but approximately one-third of the voids appeared to be glass-free. Distinguishing between glass-lined and glass-free voids is not always possible, because glass is often preferentially etched by ion milling and it can redistribute during cooling. Also, glass films can be extremely thin and thus difficult to resolve, even by TEM. However, the observation of more widespread cavitation indicated that the

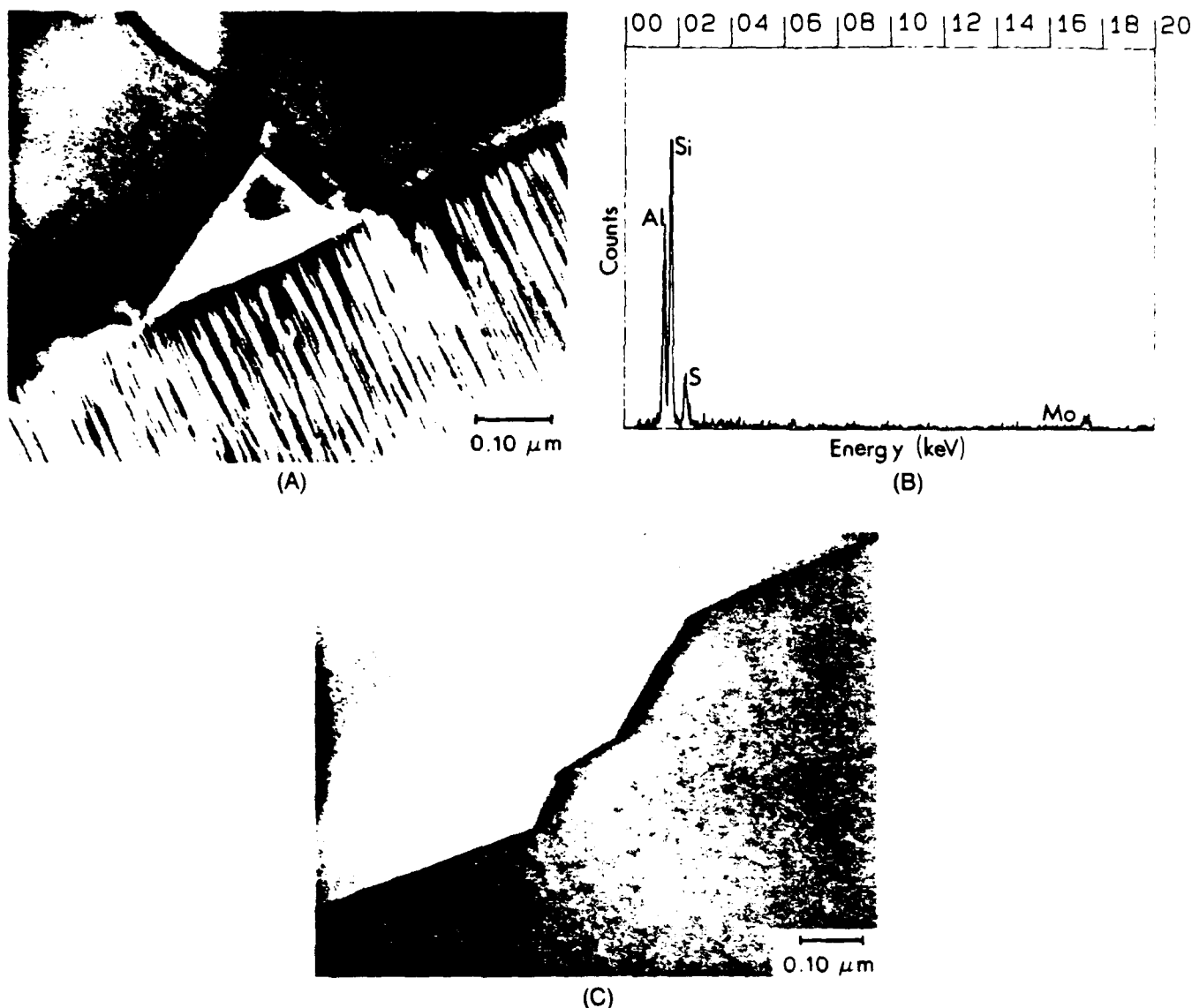


Fig. 5. Structural and chemical features of the boundary regions of the composite after creep at 1200°C in nitrogen. (A) A cavity at a grain-boundary-interface (GBI) junction. A thin layer of glass phase lines the cavity. (B) An EDS spectrum showing the composition of a typical glass phase accumulation. The elements present are primarily silicon and aluminum (and presumably oxygen) with traces of sulfur and molybdenum. (C) A corrugated alumina grain boundary.

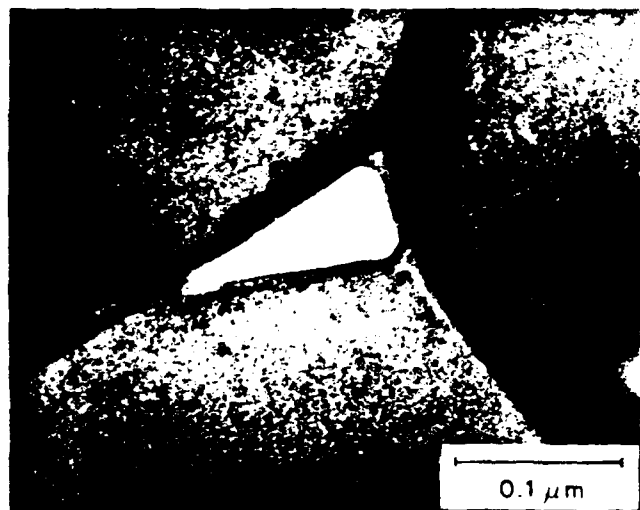


Fig. 6. A thin film of glass lining a cavity at an alumina triple grain junction after creep in nitrogen at 1300°C. The glass phase is most visible in the corners.

cavitation component of strain increased at the higher test temperature and contributed to the change in stress exponent and activation energy.

Corrugated grain boundaries were also observed in specimens tested at 1300° and 1400°C. The step height and step separation of these grain boundaries were unchanged with respect to specimens tested at 1200°C. Samples tested in nitrogen at 1400°C also exhibited voids along grain boundaries, and in rare cases the voids were accompanied by dislocations. Figure 7 shows an example of typical cavities along an alumina grain boundary. The faceted cavities are approximately 0.2 to 0.5 μm in diameter and apparently free of glass phase.

(B) *Oxidizing Ambient:* The primary microstructural difference between specimens crept in air and those tested in nitrogen was the abundance of glassy phase in the former. The development of an amorphous phase in these specimens led to a slight increase in the size and number of cavities at triple grain junctions and at sites of whisker-whisker contact. Specimens after creep exhibited glass-filled pockets and glass-lined cavities (0.5 to 1.5 μm) that occurred at GBI junctions, triple grain junctions, and at regions of whisker-whisker contact. Figure 8(A) shows a cavity at a GBI junction that was typical



Fig. 7. Faceted voids along alumina grain boundaries in specimens crept at 1400°C in nitrogen. Voids appeared to be associated with grain-boundary facets.

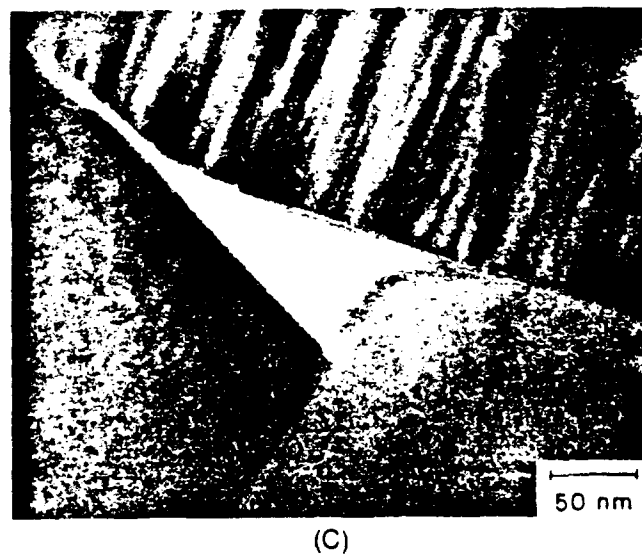
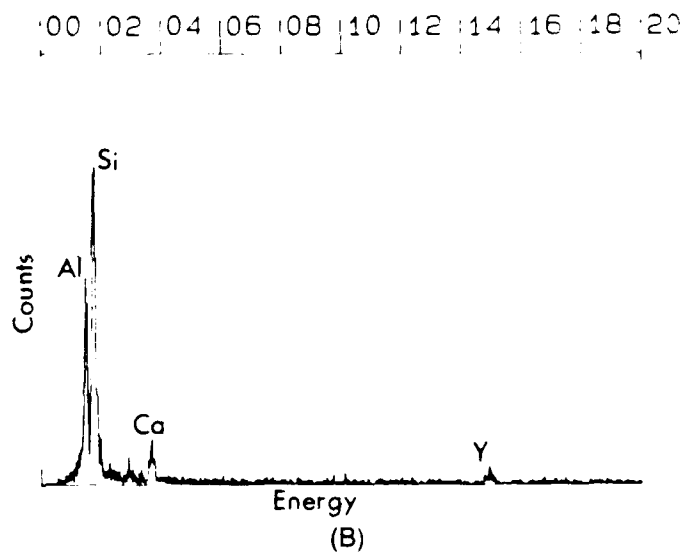
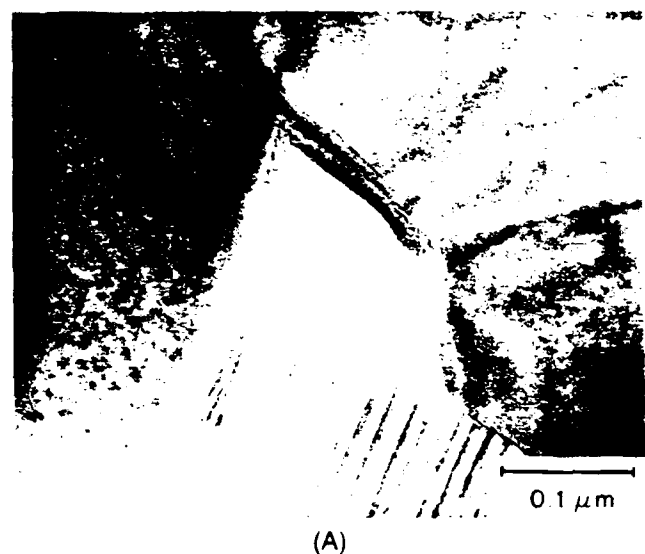


Fig. 8. Microstructural damage attributed to creep at 1300° and 1400°C in air: (A) glass-lined cavity at GBI junction in sample after creep in air at 1300°C; (B) EDS spectrum from glass phase, showing impurities of Ca and Y; (C) cavitation within glass phase accumulated at GBI junction in specimen creep-tested in air at 1400°C. Glassy ligaments bridge the separated interface.

of specimens tested in air at 1300° and 1400°C. Note that the film lining the cavity is thicker (about 10 nm) than the film shown in Fig. 5(A) where it is barely detectable. Nearly all of the cavities observed in these samples were glass-lined and assumed shapes that ranged from triangular (for smaller cavities) to polygonal (for larger ones). The EDS spectrum from the secondary phase showed primarily silicon and aluminum, with small amounts of calcium and yttrium (Fig. 8(B)). It was presumed to contain oxygen as well, although the spectrometer used could not detect oxygen. Figure 8(C) shows another cavity that developed from an accumulation of glass phase at a GBI junction. Ligaments extend across the void, indicating that the aluminosilicate phase behaved as a viscous liquid during creep deformation. Corrugated grain boundaries were also observed, although associated dislocations were not, and the overall dislocation density was negligible.

Elemental X-ray analysis was performed on over 20 glass pockets in these specimens, and the results showed distinct differences in composition. The two typical EDS spectra encountered are shown in Figs. 5(B) and 8(B). The spectrum in Fig. 5(B) shows predominantly silicon and aluminum, with small amounts of sulfur and molybdenum. The second spectrum, Fig. 8(B) shows similar concentrations of silicon and

aluminum, with small amounts of calcium and yttrium. This spectrum was typical of glass phase present in composites after creep in air. An additional constituent, although not detectable by the spectrometer, was oxygen, and the phase can be described as an aluminosilicate glass. High aluminum contents were consistently observed, and the compositions were well above the equilibrium solubility of alumina in silica. The compositions (including the impurity content) were consistent and included impurities of either molybdenum and sulfur in some cases, or calcium and yttrium in others. Glass phase of both compositions was often present in the same sample.

TEM foils sectioned near the surface of samples crept in air revealed that occasionally SiC whiskers below the surface were also oxidized. Figure 9 shows an example of a partially oxidized whisker located at a depth of approximately 1 mm below the surface of the creep sample. The whisker flank is indented and a thick film of amorphous silica has formed where the whisker has been oxidized. Samples were sectioned from different depths, and this feature generally was not observed near the center of the specimen.

IV. Discussion

(1) Creep Deformation Mechanisms

As described above, creep experiments at 1200°C in nitrogen were characterized by a stress exponent value of $n = 1$, and only subtle changes in the microstructure were observed by TEM. The microstructural changes included small cavities at GBJ junctions and grain-boundary facets. There was an insufficient number of dislocations in the matrix to support a dislocation-controlled creep mechanism. Previous creep studies of unreinforced alumina have shown that, for test conditions comparable to those used here, the material deformed by a grain-boundary diffusional creep mechanism and exhibited a stress exponent value of $n = 1$ in bending.^{22,23} Furthermore, TEM observations revealed that crept alumina was characterized by unaccommodated grain-boundary sliding, which resulted in cavities at triple grain junctions, corrugated alumina grain boundaries, and a low dislocation density.²² The similarities between observations reported here for composite samples creep-tested in compression and those reported previously for monolithic aluminas suggested that the dominant creep-deformation mechanism for the composite tested under these conditions was grain-boundary diffusional creep (Coble creep), with occasional unaccommodated sliding at interfaces and grain boundaries.

As shown in Figs. 3 and 4, as the test temperature was increased from 1200° to 1300°C in the nitrogen ambient, the strain rates showed an increased dependence on the applied

stress and an increase in activation energy. An increase in stress exponent and/or activation energy is generally attributed to the activation of a new deformation mechanism(s). For example, tensile creep tests performed on siliconized silicon carbide composites showed that an increase in stress exponent was caused by a stress-activated increase in microstructural creep damage.²⁴ At low stresses, creep deformation was controlled by dislocation glide. However, above a critical stress level, cavitation occurred at the matrix-reinforcement interface, and the stress exponent increased.²⁴ The TEM observations reported here show that, for specimens tested at 1300° to 1400°C, cavities were larger and more frequent than at 1200°C and appeared at additional sites in the microstructure, including triple grain junctions, grain boundaries, and regions of whisker-whisker contact (Figs. 5-7). The increase in creep damage was associated with the observed increases in stress exponent and activation energy. There was insufficient evidence to support a dislocation glide mechanism at either temperature.

Creep deformation mechanisms in multiphase ceramics cannot always be reliably inferred from measured values of activation energies or stress exponents. For example, the activation energy determined for creep below 1280°C was 210 kJ/mol in nitrogen and 269 kJ/mol in air, while at higher temperatures, the activation energy was 966 kJ/mol in nitrogen and 655 kJ/mol in air. These values are not entirely consistent with reported activation energies for boundary diffusion in alumina (419 kJ/mol for boundary diffusion of aluminum cations and 380 kJ/mol for oxygen anions).²² However, the TEM observations did not support a dislocation glide mechanism in the matrix, leaving diffusional creep as the most probable deformation mechanism. Note that when both lattice diffusion and grain-boundary diffusion are important, the activation energy may not be unique. Because of the extremely small grain size (1 to 2 μm), the relative contribution of boundary diffusion is expected to be greater than that of lattice diffusion.

The value of the stress exponent ($n = 3$) can be interpreted in different ways. Warshaw and Norton²³ showed that, for unreinforced aluminas, the ceramic creep rates decreased as grain size increased, and the stress exponent of large-grained alumina was approximately 4, compared to a value of $n = 1$ for fine-grained material. Jakus reported creep rates of fine-grained whisker-reinforced alumina that were similar to creep rates of large-grained alumina. He reasoned that whisker reinforcements could bond several grains into aggregates that would effectively behave as larger alumina grains, thus resulting in lower creep rates.²⁵ Chokshi and Porter, however, concluded that most of the applied load was carried by the reinforcements and compared measured stress exponents ($n = 5.2$) to those of monolithic SiC ($n = 5.7$).⁷ Cannon and Sherby suggested that an exponent of $n = 3$ could result from a combination of diffusional creep and dislocation glide processes, for which the stress exponents are expected to be $n = 1$ and $n = 5$ respectively.²⁶ A similar interpretation might be applied to the data presented here by arguing that diffusional creep of the matrix should lead to a low stress exponent ($n = 1$), while creep of the SiC reinforcements should lead to a higher stress exponent (reportedly $n = 5.7$ at 1500°C⁷). The strain rate of the composite might then be expected to show an intermediate dependence on the applied stress between that of unreinforced alumina ($n = 1$) and that of pure SiC ($n = 5.7$). However, no evidence of creep deformation was observed in the whiskers, nor was there any evidence of dislocation glide in the matrix. These observations support the previous assertion that the composite deformed by diffusional creep with unaccommodated sliding (cavitation) at 1200°C, while at higher temperatures, where the stress exponent and activation energy were higher, creep was characterized by increased microstructural damage in the form of cavitation.

The data from creep experiments at 1400°C showed an apparent stress-activated change in stress exponent from $n = 1$

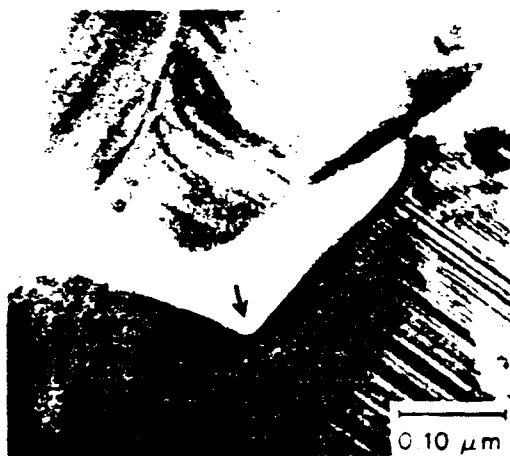


Fig. 9. Cavitation at a subsurface SiC whisker after creep in air. Thermal oxidation caused the indentation in the whisker flank and generated glass phase.

to $n = 3$ (Fig. 3). Crept microstructures (for which $n = 3$) showed that, in addition to porosity at GBI and triple grain junctions, cavities were also observed at grain-boundary facets (Fig. 7). When irregularly shaped grain boundaries slide during creep, tensile stress can develop perpendicular to the direction of sliding,²⁸ causing voids to nucleate. A plausible sequence leading to the microstructure shown in Fig. 7 would thus begin with the development of corrugated boundaries followed by void nucleation. Some of the cavitated grain boundaries were also accompanied by dislocations. However, the overall dislocation density was negligible, and it is unlikely that dislocation glide played a significant role in creep deformation at these temperatures. The presence of whisker reinforcements undoubtedly inhibited grain-boundary sliding by effectively pinning the matrix grains. However, at lower temperatures and stress levels, most of the sliding was accommodated by diffusion, while at higher temperatures and stress levels the sliding was increasingly unaccommodated. Density measurements supported this assertion, indicating that the cavitation component of creep strain increased from about 10% of the total strain at 1200°C to about 30% of the total strain at 1300°C. It was concluded that the observed threefold increase in stress exponent of the composite was associated with an increase in the cavitation component of strain, although other causes may have been involved as well. Finally, corrugated grain boundaries were also observed, indicating that although the stress exponent and strain rates increased, diffusional creep remained active at these temperatures.

(2) Oxidation Effects

The effects of the oxidizing ambient on the creep behavior of SiC-whisker-reinforced alumina can be seen in Figs. 3 and 4 and in the TEM observations of the crept microstructures (Figs. 8 and 9). Similar stress exponents and microstructures were observed for specimens tested in air and in nitrogen. For example, cavities were detected at the same types of locations in both air-tested and nitrogen-tested microstructures, and corrugated grain boundaries were observed in both. However, the glassy phase was far more prevalent in air-tested samples, and cavities were larger. In addition, the strain rates were consistently higher than for comparable stress-temperature conditions in nitrogen. This behavior was attributed to the increased amount of glassy phase that developed during creep in air. The presence of viscous amorphous films along interfaces undoubtedly facilitated grain-boundary and interface sliding, decreased the interface bond strength, and decreased the creep resistance of the composite. A layer of silica glass at grain boundaries and interfaces would also facilitate alumina dissolution-precipitation reactions.²⁹ The aluminosilicate glass film along boundaries would permit alumina to dissolve and reprecipitate, thus allowing grains to change shape and accommodate the applied stress.²⁸

Perhaps the most important effect of the oxidizing ambient on creep was the role of the vitreous phase in facilitating diffusion and cavitation. This finding is consistent with a previous investigation of creep of vitreous-bonded alumina, where it was found that cavities nucleated in the amorphous phase that existed at triple grain junctions.³⁰ In the composite, the formation of cavities at GBI junctions and at triple grain junctions allowed matrix grains to partly overcome the pinning effect of the whiskers and thus slide without accommodation. The widespread cavitation enhanced by the abundance of glass phase accounted for the increase in strain rates in air. Thus, it was concluded that the air-tested samples deformed by diffusional creep and that the boundary sliding was frequently unaccommodated, resulting in extensive cavitation.

The source of the abundant glassy phase that developed during creep in air was related to a thermal oxidation reaction that occurred during testing. Thermal oxidation experiments on similar composites have shown that the material undergoes an oxidation reaction when exposed to air at temperatures

similar to those used in the present research.¹⁴⁻¹⁶ Whiskers exposed at the surface oxidize, forming silica glass and carbon, and, if temperature (and time) are sufficient, the silica will react with alumina to form mullite. The glassy phase that developed in the air-tested specimens originated primarily from the oxidation of SiC whiskers. Under the test conditions, a silicon-rich amorphous phase formed on the surface of the composite and subsequently penetrated the composite along grain boundaries and interfaces, thereby weakening the material. Furthermore, oxygen diffusion rates were undoubtedly higher along interfaces and boundaries because of the presence of glass phase, causing oxidation of internal (subsurface) whiskers in the composite as well (Fig. 9). Other possible sources of the amorphous phase observed in crept samples include redistribution of residual sintering aids (such as MgO, Y_2O_3 , and CaO) and native oxide surface films on the SiC whiskers. The amount of glass arising from these sources was apparently much smaller than the amount formed dynamically by thermal oxidation of SiC whiskers.

The compositions of the glass phases shown in Figs. 5 and 8 were different from the composition expected from SiC oxidation alone. The presence of aluminum (Figs. 5(B) and 8(B)) implies substantial solubility of alumina in the vitreous silica. It has been reported that a binary glass can be formed containing up to 10 mol% (16 wt%) alumina and 90 mol% silica.³¹ However, the intensity of the aluminum peak in Figs. 5(B) and 8(B) corresponds to far more than 10% alumina, the solubility limit. While the characteristic X-rays of silicon will fluoresce and generate additional X-rays of aluminum from the surrounding matrix, it is unlikely that this could cause the observed Al peak intensity. Furthermore, high-resolution images did not reveal the formation of microcrystallites of alumina, silica, or mullite, indicating that the alumina was dissolved in a homogeneous glass phase. However, low-level impurities such as Mo and S (Fig. 5(B)), or Ca and Y (Fig. 8(B)) were consistently observed in the glassy accumulations, and it has been shown that these and other impurities can greatly increase the solubility of alumina in aluminosilicate glass.³² For example, the addition of small amounts of certain oxides, such as CaO, enables melts composed of up to 50 mol% alumina in silica to easily be cooled to an amorphous state.³³ The presence of impurity element(s) such as those detected in the different glass phase accumulations is likely to inhibit phase separation and emulsion during cooling, resulting in the observed homogeneous alumina-rich silicate glass.

V. Summary and Conclusions

The present investigation has shown that atmospheric effects play a strong role in the compressive creep behavior of Al_2O_3 -SiC_w composites. At 1200°C, creep in nitrogen occurred primarily by diffusion, with some unaccommodated sliding at interfaces and grain boundaries. At higher temperatures and stresses in nitrogen, the sliding was increasingly unaccommodated and the cavitation component of creep strain increased, resulting in a stronger dependence on the applied stress and a stress exponent value of 3.5. The activation energy for creep increased from 210 to 966 kJ/mol when the test temperature was increased above 1280°C. Diffusional creep continued to be an active process under all stress-temperature conditions in nitrogen. Creep experiments conducted in air showed essentially the same stress dependence, although creep rates were consistently higher. Oxidation of SiC whiskers exposed at the specimen surface led to the formation of an aluminosilicate glassy phase that subsequently penetrated along grain boundaries and interfaces and accumulated at GBI and triple grain junctions throughout the material. The formation of glass phase from thermal oxidation of SiC strongly affected the creep behavior. Glass films weakened internal boundaries in the material and increased grain-boundary diffusion rates, which contributed to accelerated

creep rates. The contribution of creep damage to the deformation process was larger for tests conducted in air than for similar tests in nitrogen.

Finally, it appears that all ceramic composites reinforced with carbide whiskers will suffer similar problems of thermal oxidation at high temperatures. Significant improvements in creep resistance would be realized by controlling the properties of the glass phase through additives that would reduce the viscosity of the glass or enhance devitrification, or by the use of protective coatings. Alternatively, the development of oxidation-resistant reinforcements such as oxides, nitrides, or silicides would be beneficial to the advancement of ceramic matrix composites for high-temperature structural applications. Successful solutions would depend on the stress-temperature conditions involved in the application and on the particular service environment.

References

- ¹R. Warren and V. K. Sarin, pp. 571-614 in *Application of Fracture Mechanics to Composite Materials*, Edited by K. Friedrich, Elsevier, Amsterdam, Netherlands, 1989.
- ²P. F. Becher and G. C. Wei, "Toughening Behavior of SiC-Whisker-Reinforced Alumina," *J. Am. Ceram. Soc.*, **67** [12] C-267-C-269 (1984).
- ³P. F. Becher and G. C. Wei, "Development of SiC-Whisker-Reinforced Ceramics," *Am. Ceram. Soc. Bull.*, **64** [2] 298-304 (1985).
- ⁴S. C. Samanta and S. Musikant, "SiC Whisker-Reinforced Ceramic Matrix Composites," *Ceram. Eng. Sci. Proc.*, **6** [7-8] 663-72 (1985).
- ⁵P. D. Shalek, J. J. Petrovic, G. F. Hurley, and F. D. Gac, "Hot-Pressed SiC Whisker/Si₃N₄ Matrix Composites," *Am. Ceram. Soc. Bull.*, **65** [2] 351-56 (1986).
- ⁶F. D. Gac and J. J. Petrovic, "Feasibility of a Composite of SiC Whiskers in a MoSi₂ Matrix," *J. Am. Ceram. Soc.*, **68** [8] C-200-C-203 (1985).
- ⁷A. H. Chokshi and J. R. Porter, "Creep Deformation of an Alumina Matrix Composite Reinforced with Silicon Carbide Whiskers," *J. Am. Ceram. Soc.*, **68** [6] C-144-C-145 (1985).
- ⁸S. R. Nutt, P. Lipetzky, and P. F. Becher, "Creep Deformation of Alumina-SiC Composites," *Mater. Sci. Eng.*, **A126**, 165-72 (1990).
- ⁹K. Jakus and S. V. Nair, "Nucleation and Growth of Cracks in SiC Alumina Composites," *Compos. Sci. Technol.*, **37**, 279-97 (1990).
- ¹⁰R. D. Nixon, D. A. Koester, S. Chevacharoenkul, and R. F. Davis, "Steady-State Creep of Hot-Pressed SiC Whisker-Reinforced Silicon Nitride," *Compos. Sci. Technol.*, **37**, 313-28 (1990).
- ¹¹A. R. de Arellano-Lopez, F. L. Cumbre, A. D. Dominguez-Rodriguez, K. C. Goretti, and J. L. Routbort, "Compressive Creep of SiC-Whisker-Reinforced Al₂O₃," *J. Am. Ceram. Soc.*, **73** [5] 1297-300 (1990).
- ¹²K. Xia and T. G. Langdon, "The Mechanical Properties at High Temperatures of SiC Whisker-Reinforced Alumina," *Mater. Res. Soc. Symp. Proc.*, **120**, 265-70 (1988).
- ¹³P. Lipetzky, S. R. Nutt and P. F. Becher, "Creep Behavior of an Al₂O₃-SiC Composite," *Mater. Res. Soc. Symp. Proc.*, **120**, 271-77 (1988).
- ¹⁴J. R. Porter and A. H. Chokshi, "Creep Performance of SiC-Whisker Reinforced Alumina," p. 913 in *Ceramic Microstructures 1986*, Edited by J. A. Pask and A. G. Evans, Plenum Press, New York, 1988.
- ¹⁵F. Lin, T. Marieb, A. Morrone, and S. R. Nutt, "Thermal Oxidation of Alumina-SiC Whisker Composites: Mechanisms and Kinetics," *Mater. Res. Soc. Symp. Proc.*, **120**, 323-32 (1988).
- ¹⁶K. L. Luthra and H. D. Park, "Oxidation of Silicon Carbide-Reinforced Oxide-Matrix Composites at 1375° to 1575°C," *J. Am. Ceram. Soc.*, **73** [4] 1014-23 (1990).
- ¹⁷J. S. Reed, *Introduction to the Principles of Ceramic Processing*, p. 323, Wiley, New York, 1988.
- ¹⁸C. H. Carter, C. A. Stone, R. F. Davis, and D. R. Schaub, "A High Temperature, Multi-Atmosphere, Constant Stress Compressive Creep Apparatus," *Rev. Sci. Instrum.*, **51** [10] 1352-57 (1980).
- ¹⁹W. R. Cannon and R. L. Coble, *Deformation of Ceramic Materials*, Edited by R. C. Bradt and R. E. Tressler, Plenum Press, New York, 1975.
- ²⁰W. R. Cannon and T. G. Langdon, "Review: Creep of Ceramics, Part 2," *J. Appl. Sci.*, **23**, 1-20 (1980).
- ²¹K. J. Morrissey and C. B. Carter, "Faceted Grain Boundaries in Al₂O₃," *J. Am. Ceram. Soc.*, **67** [4] 292-301 (1984).
- ²²W. R. Cannon, W. R. Rhodes, and A. H. Heuer, "Plastic Deformation of Fine Grained Alumina. I. Interface-Controlled Diffusional Creep," *J. Am. Ceram. Soc.*, **63** [1-2] 46-53 (1980).
- ²³S. I. Warshaw and F. H. Norton, "Deformation Behavior of Polycrystalline Aluminum Oxide," *J. Am. Ceram. Soc.*, **45** [10] 479-86 (1962).
- ²⁴D. F. Carroll and R. E. Tressler, "Effect of Creep Damage on the Tensile Creep Behavior of a Siliconized Silicon Carbide," *J. Am. Ceram. Soc.*, **72** [1] 49-53 (1989).
- ²⁵K. Jakus and S. V. Nair, "Elevated Temperature Crack Growth in SiC Whisker Reinforced Alumina," *Ceram. Eng. Sci. Proc.*, **9** [7-8] 767-76 (1988).
- ²⁶W. R. Cannon and O. D. Sherby, "Third-Power Stress Dependence in Creep of Polycrystalline Nonmetals," *J. Am. Ceram. Soc.*, **56** [3] 157-60 (1973).
- ²⁷C. H. Carter, R. F. Davis, and J. Bentley, "Kinetics and Mechanisms of High-Temperature Creep in Silicon Carbide. I. Reaction-Bonded," *J. Am. Ceram. Soc.*, **67** [6] 409-17 (1984).
- ²⁸J. H. Schrieber and P. M. Hazzledine, "Sliding of Irregularly Shaped Grain Boundaries," *J. Mater. Res.*, **5** [3] 563-69 (1990).
- ²⁹S. M. Wiederhorn, B. J. Hockey, R. F. Krause, and K. Jakus, "Creep and Fracture of a Vitreous-Bonded Alumina," *J. Mater. Sci.*, **21**, 819-24 (1986).
- ³⁰K. Jakus, S. M. Wiederhorn, and B. J. Hockey, "Nucleation and Growth of Cracks in Vitreous-Bonded Aluminum Oxide at Elevated Temperatures," *J. Am. Ceram. Soc.*, **69** [10] 724-31 (1986).
- ³¹J. F. MacDowell and G. H. Beall, "Immiscibility and Crystallization in Al₂O₃-SiO₂ Glasses," *J. Am. Ceram. Soc.*, **52** [3] 17-25 (1969).

MECHANICALLY INDUCED RESIDUAL STRESSES IN Al/SiC COMPOSITES

G.L. Povirk¹, M.G. Stout², M. Bourke², J.A. Goldstone²,
A.C. Lawson², M. Lovato², S.R. MacEwen³, S.R. Nutt¹ and A. Needleman¹

¹Division of Engineering, Brown University
Providence, Rhode Island 02912 USA

²Los Alamos National Laboratory
Los Alamos, New Mexico 87545 USA

³Alcan International Ltd., Kingston Research and Development Centre
Kingston, Ontario K7L 5L9 Canada

Introduction

Mechanically induced residual stresses are an inherent feature of permanently deformed metal-matrix composites. The presence of hard reinforcement particles promotes non-homogeneous flow in the material, resulting in residual stresses when the applied loads are removed. Several distinct approaches have been used in attempts to quantify thermally and mechanically induced residual stresses in metal-matrix composites. One approach has been to assume that the composite consists of a periodic array of whiskers embedded throughout the matrix [1]. With this assumption, a boundary value problem can be formulated on a single unit cell and solved by use of the finite element method. A second approach uses modified techniques originally developed by Eshelby [2] to estimate residual stresses for composites reinforced by ellipsoidal inclusions [3].

The main objective of the present investigation is to compare predicted average residual elastic strains with those measured by neutron diffraction for Al/SiC composites subjected to a rapid quench followed by different loading histories. Similar comparisons of neutron diffraction measurements of thermally induced residual strains and elastic calculations, sometimes including a simple model for creep relaxation, were performed on a variety of composite materials by Majumdar et al. [4]. Other objectives are to compare the results of finite element and Eshelby model predictions of residual strains and to ascertain the effect of inclusion shape on predicted values of average residual elastic strains.

Experimental

The composite studied was a 2009 aluminum alloy (Al-3.8%Cu-1.3%Mg-0.02%Fe) reinforced with 15 vol% silicon carbide whiskers, obtained from the Advanced Composite Materials Corp. in Greer, S.C. The 2009 matrix alloy was specifically designed for use in metal-matrix composites. The samples were solutionized for 1 hour at a temperature of 493°C, quenched in water, and then deformed in uniform tension or compression to varying levels of plastic strain. In one case, a specimen was strained until fracture. The specimens were subsequently stored in liquid nitrogen to prevent recovery in the aluminum matrix. Approximately 8 hours prior to a neutron diffraction experiment, samples were returned to room temperature. To ascertain the mechanical properties of 2009 aluminum at these temperatures, tensile tests were also performed on the unreinforced matrix in liquid nitrogen (-196°C), in a solution of dry ice and methyl alcohol (-75°C), and at room temperature. The unreinforced alloy received the identical solutionizing treatment given the composite, although this does not necessarily lead to the same microstructural state as is in the composite matrix [5].

The neutron diffraction measurements were performed on the Neutron Powder Diffractometer at the Manuel Lujan, Jr. Los Alamos Neutron Scattering Center (LANSCE), located at the Los Alamos National Laboratory. This facility utilizes a high-intensity pulsed spallation source. In addition to the

composite samples, experiments were also performed on the unreinforced alloy and on unrestrained silicon carbide whiskers to determine stress-free lattice constants. Specimens were placed in the diffractometer with the deformation axis in the diffraction plane and oriented at 45 degrees to the incident neutron beam. The samples were 6.35 mm in diameter and 38.1 mm in length. Time-of-flight diffraction patterns were collected in each of two opposed detectors placed at ± 90 degrees with respect to the incident beam over an eight hour (typical) period. The diffraction vectors for these patterns were, respectively, parallel and perpendicular to the deformation axis.

Bragg reflections in each spectrum were fitted individually to obtain interplanar spacings. In addition, lattice parameters were obtained for the aluminum matrix by use of Rietveld profile refinement [6]. One advantage to profile refinement is that all the lattice reflections contribute to the determination of the lattice parameter. Once the interplanar spacings are obtained from the diffraction patterns, the lattice strains are then given by the relations

$$\epsilon_{hkl} = \frac{d_{hkl} - d_{hkl}^0}{d_{hkl}^0} \quad (1)$$

where, for example, d_{hkl} represents matrix lattice spacings in the composite and d_{hkl}^0 represents corresponding lattice spacings in the unreinforced alloy, and ϵ_{hkl} is the calculated matrix strain for a given lattice plane. For the profile refinements, the strain is calculated by replacing values of interplanar spacings in (1) by the values of the lattice parameters.

Theory

Withers et al. [3] developed an analytical method that uses solutions for ellipsoidal inclusions provided by Eshelby [2] to determine the residual stress states in thermally and mechanically deformed composites. In reference [3] relations are developed that express the inclusion transformation strain in terms of the plastic deformation undergone by the composite. From the calculated transformation strain, the average residual stresses and strains are predicted. The chief advantage to this approach is that no extensive computing is required.

Although axisymmetric unit cell based finite element calculations require larger amounts of computer time (but still considerably less than a full three dimensional simulation), they can incorporate more general inclusion geometries and material properties. For the computations here, the methodology of reference [7] is used. Briefly, the material is modelled as a periodic array of hexagonal cylinders, each consisting of the aluminum alloy with a silicon carbide fiber embedded in the center. The hexagonal cylinder can then be approximated as a circular cylinder, so that the problem is rendered axisymmetric. In addition, because of symmetry, only one quadrant of the cylinder needs to be analyzed. Both right circular cylindrical and ellipsoidal reinforcements are considered; for the calculations here the aspect ratio of the unit cell and of the reinforcement is taken to be four.

The analysis occurs in several distinct steps, each corresponding to those taken in the experiments. First, a temperature history is applied which simulates a quench of the composite in ice water. In computing the thermally-induced residual stresses, the material is taken to be stress-free at a uniform temperature of 350°C. Prior studies [7] have shown negligible dependence of computed residual stresses on solutionizing temperatures at or above 350°C because of the low flow strengths of aluminum alloys at these temperatures. Once the material is quenched, the mechanical response of the composite subject to uniaxial tension or compression along the fiber axis is simulated. The unit cell is then unloaded so that the net stresses vanish on the cell walls, and is subsequently cooled to liquid nitrogen temperature (-196°C). Finally, the composite is returned to room temperature.

Completing the equations for either method requires specifying the appropriate constitutive response for both phases, although only the elastic constants are required for the approach based on Eshelby solutions [3]. The silicon carbide whiskers are taken to be elastic and the aluminum matrix is modelled as an isotropically hardening elastic-viscoplastic solid. The uniaxial plastic response of the matrix is given by

$$\sigma = \sigma_0 \left(\frac{\dot{\epsilon}^p}{\dot{\epsilon}_0} \right)^m \left[\frac{\epsilon^p}{\epsilon_0} + 1 \right]^N \quad (2)$$

with a reference strain rate of $\dot{\epsilon}_0 = 0.002s^{-1}$, a reference strain of $\epsilon_0 = 0.004$, and a strain rate hardening exponent of $m = 0.004$. Poisson's ratio was taken to be $\nu = 0.3$, and the coefficient of

thermal expansion was $\alpha = 24 \times 10^{-6} \text{ }^{\circ}\text{K}^{-1}$. The reference strength σ_0 , strain hardening exponent N , and Young's modulus E were considered to be functions of temperature. Although these values were known at lower temperatures from our own experiments, material data was not available for 2009 aluminum at higher temperatures. The properties at high temperatures were assumed to be those of 6061-T6 aluminum [8], which has roughly the same flow behavior as 2009 aluminum at room temperature. The constitutive relation was generalized to multi-axial states by the usual procedure of replacing the stress and plastic strain appearing in (2) with their respective von Mises equivalents. The property values of β silicon carbide were taken to be $E = 470 \text{ GPa}$, $\nu = 0.19$, and $\alpha = 4.7 \times 10^{-6} \text{ }^{\circ}\text{K}^{-1}$ [9].

Results and Discussion

The stress vs. strain curves in tension and in compression predicted by the finite element simulations of a unit cell reinforced with cylindrical fibers are compared with experimental data in Figure 1. The test specimens exhibit significantly higher flow strengths in compression, in agreement with other published reports [10,11]. The calculations predict nearly identical composite flow strengths by 3% strain, suggesting that damage mechanisms not included in the computations may cause the observed differences between the tensile and compressive stress-strain behavior.

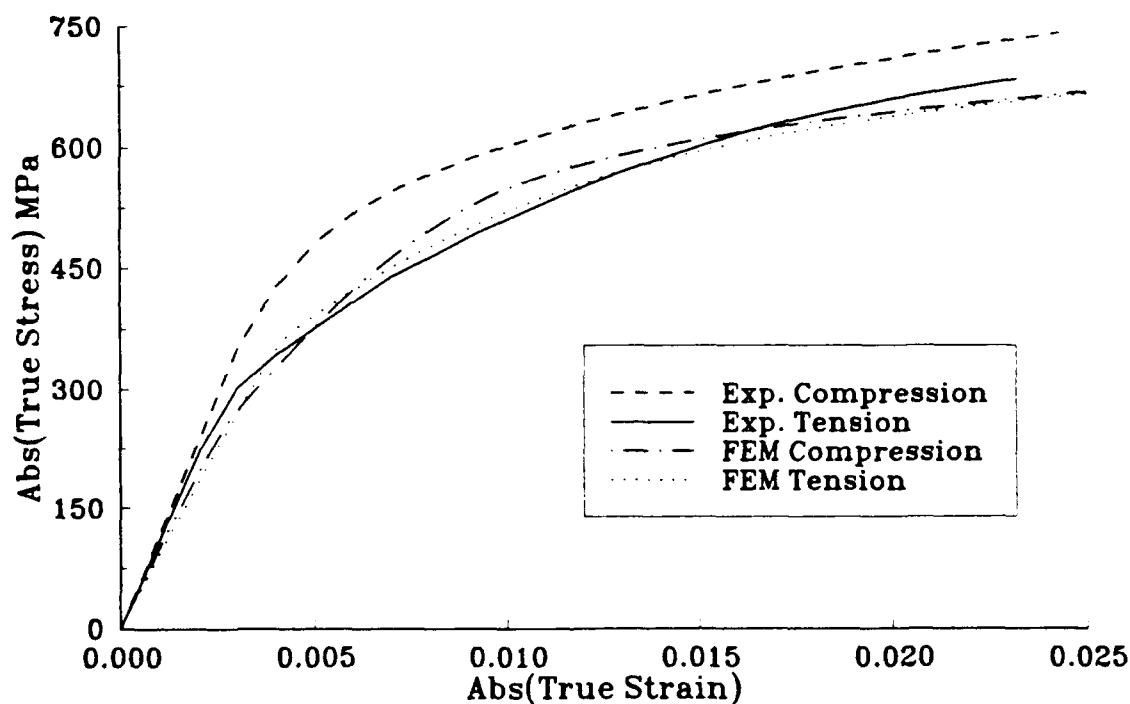


Fig. 1 Comparisons of the experimental and predicted stress vs. strain response in tension and in compression of a 2009 Al/ 15 vol% SiC composite.

The predicted levels of residual axial strain in the matrix as a function of composite plastic deformation for the three different models considered here are shown in Figure 2. The analytical method of Withers [3] et al. (here assuming no thermal residual stresses) gives a linear dependence of residual strain on plastic deformation. For comparative purposes, we also derived solutions for a simple radially-loaded composite spherical shell model, assuming an incompressible, elastic-perfectly plastic matrix reinforced with a spherical elastic inclusion. This model also predicts a linear relationship between residual strain and composite plastic strain. In contrast, the finite element solutions predict a non-linear dependence. Finite element calculations with ellipsoidal inclusions predict roughly 50 percent lower residual elastic strains compared to those obtained with a cylindrical fiber.

The residual strains measured by neutron diffraction are compared with the finite element predictions assuming cylindrical reinforcements in Figure 3. The solutions have excellent qualitative

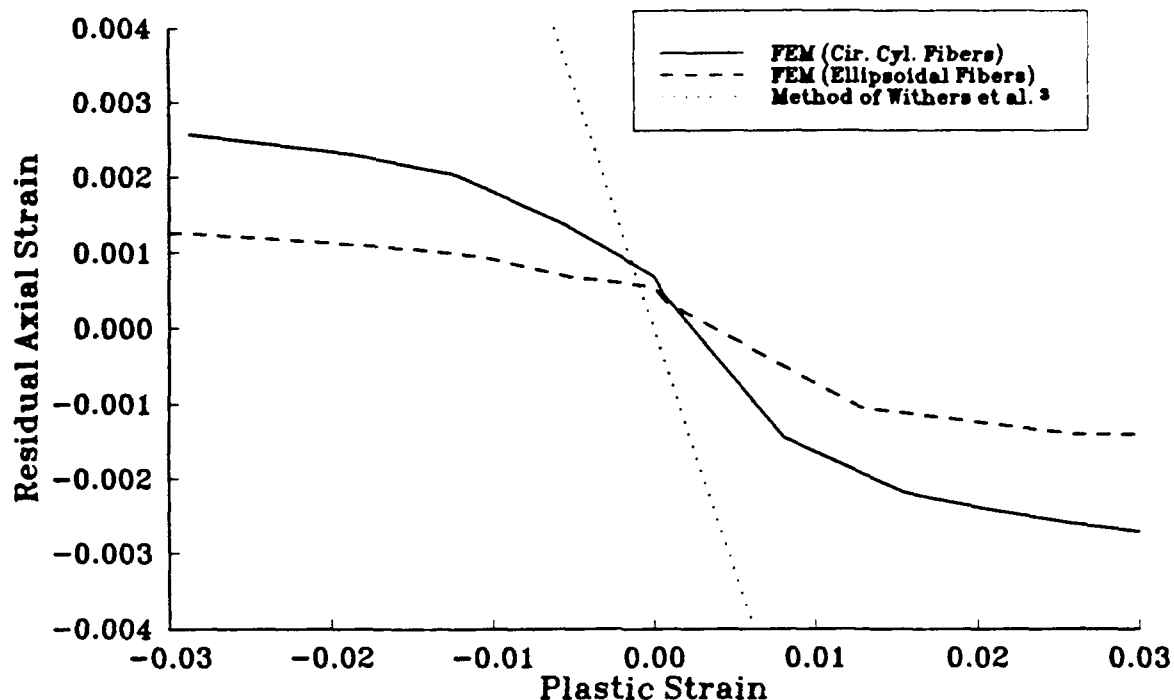


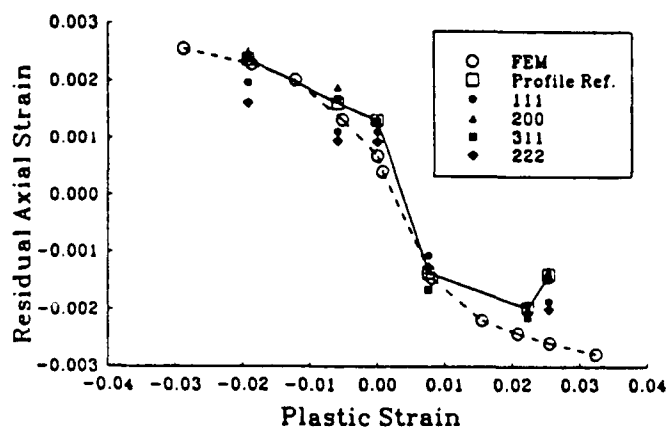
Fig. 2 Comparisons of three different model predictions of average matrix elastic residual strain in the axial direction vs. imposed composite plastic deformation. Thermal residual stresses were not included when implementing the method of Withers et al. [3].

agreement with the experimental curves, and very good quantitative agreement is found for the residual elastic strains in the aluminum matrix. Note that the thermal residual strains are quickly dominated by the residual strains generated by even relatively small levels of composite plastic deformation. This behavior is in agreement with calculations performed in [7], which demonstrated that composites with and without thermally induced residual stresses included in the analysis had nearly identical stress states after small amounts of deformation. Also note that the residual elastic strains are lower in the fractured specimen (the specimen with the greatest plastic strain), which would suggest that the composite experienced significant damage in the latter stages of the tensile test.

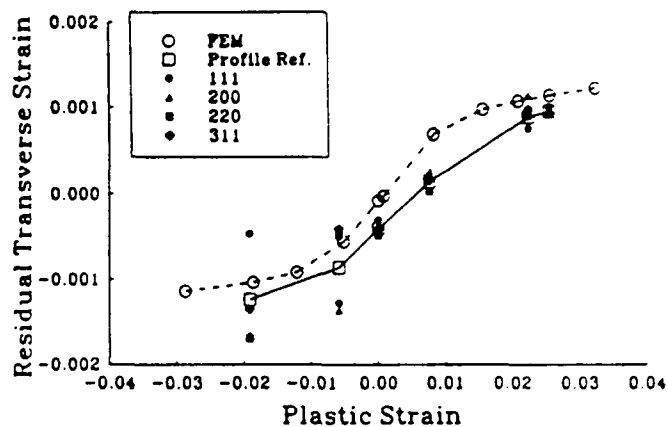
Only lattice spacings for one plane of silicon carbide could be measured experimentally in each direction because of the alignment of whiskers in the composite. Although the trend of residual axial strain in the silicon carbide reinforcements was correctly predicted by the finite element calculations, the magnitudes of residual strain were consistently underestimated. In contrast, predicted magnitudes of residual strain in the transverse direction were greater than the measured values. The reasons for these discrepancies has not been conclusively identified. One possibility is that the measurements of whisker axial strains involved only perfectly aligned whiskers, and therefore may not have been representative of the average state of the reinforcements. Another possible reason could be attributed to uncertainties in the elastic properties of the whiskers. In addition to effects of elastic anisotropy, reported values of elastic moduli for β silicon carbide in the $\langle 111 \rangle$ direction range from 352 GPa [12] to over 500 GPa [13]. In contrast, the aluminum matrix is nearly isotropic and its elastic constants are well characterized. Finally, the silicon carbide diffraction peaks were often irregular in shape and intensity, and consequently lattice spacings obtained using the curve-fitting algorithms exhibited greater uncertainty than those obtained from the aluminum diffraction peaks. These irregularities may be associated with the high density of grown-in defects present in the whiskers [14].

Conclusions

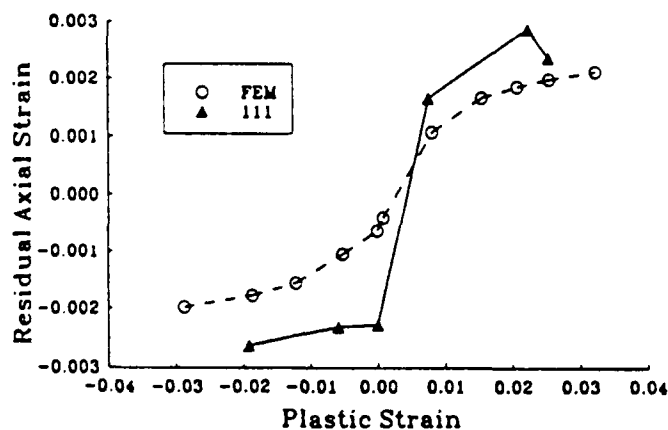
Mechanically induced residual stresses in Al/SiC composites were studied with analytical and numerical models, and with neutron diffraction experiments that measured average residual elastic strains in the fibers and matrix. The method of Withers et al. [3] predicted a linear dependence



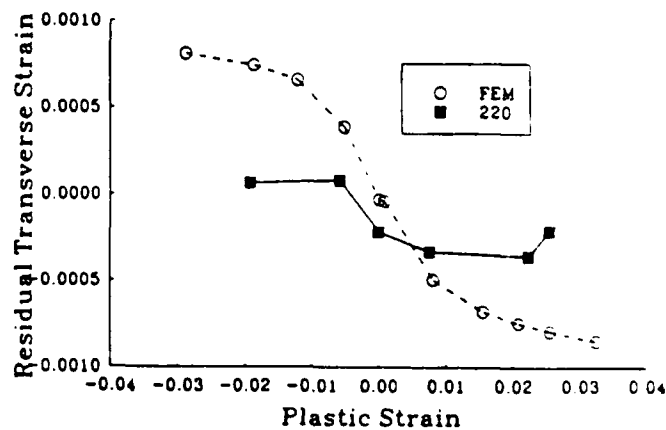
(a)



(b)



(c)



(d)

Fig. 3 Comparisons of average residual elastic strains vs. composite plastic strain as measured by neutron diffraction and predicted by finite element calculations with cylindrical reinforcements for (a) the aluminum matrix in the axial direction, (b) the aluminum matrix in the transverse direction, (c) the silicon carbide whiskers in the axial direction, and (d) the silicon carbide whiskers in the transverse direction. Included in the aluminum data are strains measured for individual lattice planes and by Rietveld profile refinement [6].

of residual elastic strains on the imposed plastic deformation, in disagreement with experimental results. In that study, the authors speculated that the observed non-linear dependence on composite plastic deformation was caused by room temperature diffusional relaxation of the aluminum matrix. The finite element calculations suggest that this is unlikely, since good quantitative agreement with experiments was observed for the aluminum matrix without any diffusional terms included in the model. Furthermore, the finite element solutions also suggest that inclusion geometry significantly affects the values of even average field quantities.

Only qualitative agreement was obtained for the average residual strains in the silicon carbide whiskers. Possible reasons for the discrepancies include fiber misorientation, poorly characterized elastic moduli for the silicon carbide, or errors induced by inconsistent diffraction peaks. Because the whiskers are essentially rigid in comparison to the plastically deforming aluminum alloy, model predictions of matrix residual strains are relatively insensitive to reinforcement elastic properties. The close correlation of the numerical model with neutron diffraction measurements of the aluminum matrix suggest that it may be possible to predict microstructural-level stresses with unit cell, continuum-based models using the finite element method. Future work will address residual stresses in Al/SiC particulate composites and the effects of more complex loading paths.

Acknowledgements

Support from the Office of Naval Research through contract numbers N00014-86-K-0125 and N00014-89-J-3054 is gratefully acknowledged. The computations were carried out at the Pittsburgh Supercomputing Center. The Manual Lujan, Jr. Neutron Scattering Center is a national user facility funded by the United States Dept. of Energy, Office of Basic Energy Research. We are grateful to Dr. J.A. Walker of the Advanced Composite Materials Corp. for supplying the materials and for technical advice and assistance.

References

- [1] G.L. Povirk, A. Needleman, and S.R. Nutt, *Mat. Sci. Eng. A125*, 129 (1990).
- [2] J.D. Eshelby, *Proc. R. Soc. 241A*, 376 (1957).
- [3] P.J. Withers, W.M. Stobbs and O.B. Pederson, *Acta Metall.* 37, 3061 (1989).
- [4] S. Majumdar, J.P. Singh, D. Kupperman, A.D. Krawitz, *J. Eng. Mat. & Tech.* 113, 51 (1991).
- [5] T. Christman and S. Suresh, *Acta Metall.* 36, 1691 (1988).
- [6] R.B. Von Dreele, J.D. Jorgensen, C.G. Windsor, *J. Appl. Crystall.* 15, 581 (1982).
- [7] G.L. Povirk, A. Needleman, and S.R. Nutt, *Mat. Sci. Eng. A132*, 31 (1991).
- [8] *Metals Handbook 9th Edition*, vol. 2, American Society of Metals, Metals Park, Ohio, 1979.
- [9] Battelle Memorial Institute, *Engineering Properties of Selected Ceramic Materials*, American Ceramic Society, Columbus, Ohio, 1966.
- [10] R.J. Arsenault and M. Taya, *Acta Metall.* 35, 651 (1987).
- [11] T.J. Warner and W.M. Stobbs, *Acta Metall.* 37, 2873 (1989).
- [12] P. Predecki, A. Abuhasan, and C.S. Barrett, *Adv. in X-Ray Analy.* 31, 231 (1988).
- [13] J.J. Petrovic, J.V. Milewski, D.L. Rohr, F.D. Gac, *J. Mat. Sci.* 20, 1167 (1985).
- [14] S.R. Nutt, *J. Am. Ceram. Soc.* 71, 149 (1988).

On Microstructural Evolution and Micromechanical Modelling of Deformation of a Whisker-reinforced Metal-Matrix Composite*

T. CHRISTMAN, A. NEEDLEMAN, S. NUTT and S. SURESH

Division of Engineering, Brown University, Providence, RI 02912 (U.S.A.)

Received June 1, 1988

Abstract

The precipitation characteristics, the mechanisms of accelerated aging, and the variation of uniaxial tensile stress-strain behavior in response to controlled variations in matrix microstructure were investigated for a 2124 Al-SiC whisker composite. The yield strength of the composite was found to be independent of matrix aging condition. However, the overall ductility decreased monotonically with an increase in aging time. A finite element analysis of the constitutive response of the composite is presented. The results of these calculations, as well as the predictions of several models for composite strengthening available in the literature, were compared with the experimental results. The presence of brittle whiskers in aluminum leads to a significant build-up of hydrostatic stresses in the matrix during plastic deformation. Void formation in the matrix of the composite as well as at the whisker-matrix interface appears to play an important role in controlling the overall failure mechanisms. Transmission electron microscopy observations of void formation at whisker ends are described for composite specimens strained in tension at room temperature and at 300 °C. A detailed discussion of matrix deformation and interfacial debonding is presented in an attempt to identify the origins of low ductility in discontinuously reinforced metal-ceramic composites.

1. Introduction

With recent advances in processing technology, the ability to produce, in economically feasible quantities, a wide range of metal-matrix composites is increasing dramatically. Metals reinforced with brittle particles, often referred

to as discontinuously reinforced metal-matrix composites, constitute a large portion of these advanced materials. Particle-reinforced metal-matrix composites are both machinable and workable using conventional processing techniques, and the manufacturing of these materials can easily be scaled up to production quantities. Experimental results of stress-strain relations for these materials have been reported previously [1-5], although the effects of systematic variations in the matrix microstructure on the overall composite properties have not been examined. Recent work has demonstrated that aging-induced precipitation and microstructural evolution in the matrix of whisker-reinforced composite materials can be significantly accelerated compared with those of the unreinforced matrix material subjected to identical heat treatments [6-8]. These results indicate that conventional heat treatments for unreinforced commercial aluminum alloys should not be directly applied to the microstructural design of composite materials although this is often the practice [1, 5, 9, 10]. A thorough examination of microstructural evolution in the matrix of the composite and its effects on overall mechanical behavior is critical to a more complete understanding of the constitutive response and to the evaluation of composite strengthening theories. The low ductility exhibited by discontinuously reinforced metal-matrix composites is the primary obstacle preventing their introduction into many structural applications. Yet the influence of controlled matrix microstructural variations on the strain-to-failure of whisker-reinforced metal-matrix composites remains poorly understood. This report will focus on experimental observations and finite element analysis of the effects of matrix microstructural variations on the uniaxial stress-strain response of a discontinuously reinforced metal-matrix composite in an attempt to better understand the failure mechanisms.

*Paper presented at the symposium on Interfacial Phenomena in Composites: Processing, Characterization, and Mechanical Properties, Newport, RI, June 1-3, 1988.

The material selected for this study was a 2124 Al-15 wt.%(13 vol.%)SiC whisker reinforced metal-matrix composite obtained from ARCO Chemicals, Greer SC, produced using powder metallurgy techniques. The 2124 Al matrix material had a nominal composition, in weight percent, of 4%Cu-2%Mg-0.4%Mn, with the balance Al. For comparison where appropriate, an unreinforced alloy of 2124 Al, that was identically processed from the same powder batch and subjected to identical solutionizing and aging treatments, was also studied. The whiskers used in this study were the highest quality available and were classified as F-9. The average dimensions of the whiskers before processing were 0.5 μm in diameter and 25 μm in length. However, due to the severe deformation involved in processing of the composite material, significant breakage of the whiskers occurred and the average length of the whiskers in the as-extruded material was about 2.5 μm . A systematic microstructural characterization and aging study of the same extruded bars of the composite and control alloy was performed by Christman and Suresh [6] and will be briefly reviewed in a later section (the reader is referred to the original paper for a more complete discussion). Furthermore, composite damage mechanisms operative during uniaxial tensile tests at high temperatures will be discussed and compared with damage mechanisms at room temperature.

A finite element unit cell model was used to predict the uniaxial stress-strain response of the composite material as a function of matrix microstructural variations. The model approximates the stress-strain response of a single, rigid cylindrical inclusion in an elastic power-law hardening viscoplastic matrix material. The matrix and whisker parameters were taken directly from experiments (when possible), thereby minimizing the number of adjustable variables. The experimental observations were compared with the numerical predictions and the implications of the results are discussed in the context of the mechanisms responsible for the high values of yield strength and the low values of ductility displayed by the material.

2. Microstructural evolution

Recently, Christman and Suresh [6] conducted a study of the microstructural evolution and aging kinetics in the 2124 Al-SiC whisker composite

and control alloy used in this study, utilizing analytical transmission electron microscopy techniques, matrix microhardness measurements and conductivity measurements. The aim of the work reported in ref. 6 was to examine the effects on the matrix of the composite produced by the introduction of the whiskers in controlled microstructures by a comparison of reinforced and unreinforced materials.

The composite and control alloy were received in the as-extruded condition, solution-treated at 504 °C for 4 h, water quenched, and subsequently aged at 177 °C for various times. The microstructural condition of the matrix material was determined by microhardness measurements (Fig. 1a) and by analytical electron microscopy. With the addition of the SiC whiskers, the peak aging time of the matrix of the composite is drastically reduced from 12 h for the control alloy to about 3 h. Another interesting feature of this

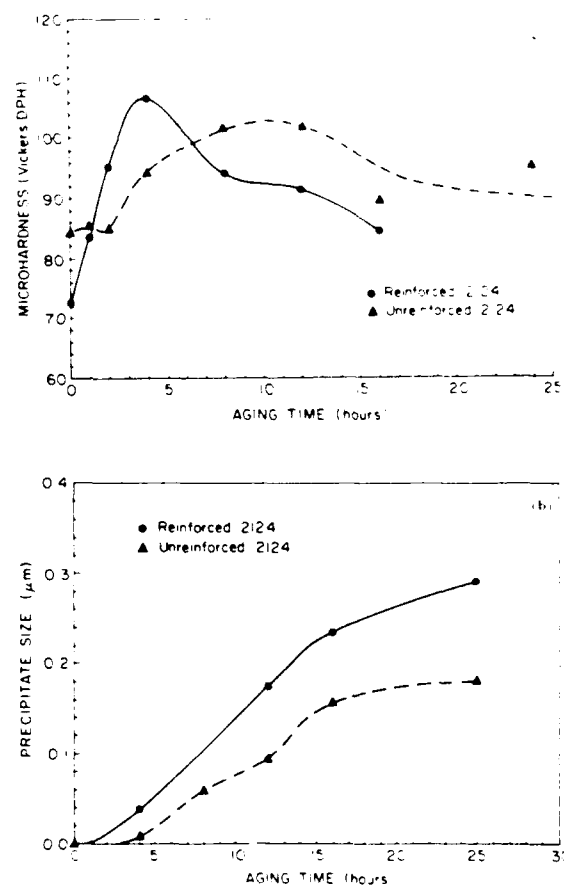


Fig. 1 The variation of a microhardness and b precipitate size with aging time after ref. 6.

graph is that there is no appreciable vertical shift in the microhardness values, that is the composite matrix is not significantly harder than the unreinforced material. This result suggests that it would be possible to use the bulk mechanical properties of the control alloy for the matrix properties of the composite in theoretical calculations of the constitutive response of the composite, with proper adjustments for changes in the aging curves. This inference has a strong bearing on the evaluation of composite strengthening theories which will be discussed in a later section.

The transmission electron microscopy (TEM) results showed that the age-hardening precipitates, S' , evolve into corrugated sheets after nucleating on dislocations and growing in the three preferential (001) directions. This type of precipitation sequence is typical of Al-Cu-Mg alloy systems and is well documented in the literature [11-13]. There is little preferential precipitation or precipitate-free zones at or near the whisker-matrix interface. The rate of nucleation of the precipitates, however, was different between the reinforced and unreinforced materials. The reinforced material showed evidence of S' nucleation after less than 1 h of artificial aging at 177 °C, whereas the unreinforced material required up to 4 h of aging at this temperature before any S' could be detected, Fig. 1 b.

The accelerated aging of the composite matrix material is aided by a decrease in the incubation time for the nucleation of age-hardening precipitates. The large thermal contraction mismatch between the aluminum matrix and the SiC whiskers gives rise to residual stresses upon cooling from the solutionizing temperature. Dislocations are punched out from whisker ends during cooling to relieve part of the residual stresses at the interface. For 2124 Al-13.2vol.%SiC composite, the dislocation punching distance calculated from ref. 14 is sufficiently large to cover the majority (approximately 75%) of the matrix with excess dislocations. Transmission electron microscopy studies by Christman and Suresh [6] indicate that the dislocations in the matrix of the composite serve as nucleation sites for the formation of S' precipitates during the aging of the composite. This facilitates the attainment of peak matrix hardness at much shorter times than in the control alloy.

The theory for accelerated aging listed above is supported by a wide variety of evidence (Christman and Suresh [6]):

(1) TEM studies of the composite material and unreinforced alloy reveal increased dislocation density in the matrix of the composite.

(2) TEM studies also reveal that the strengthening precipitates nucleate preferentially along dislocation lines.

(3) Little preferential precipitation or precipitate free zone at or near the whisker interfaces was observed.

(4) Quantitative analysis of the growth kinetics of the strengthening precipitates for both the reinforced and unreinforced materials shows a shift in nucleation time but not in growth kinetics.

(5) Measurements of changes in electrical conductivity are consistent with the proposed model.

(6) Cold working of the unreinforced material also produces an accelerated aging effect.

(7) Recent *in situ* TEM experiments have demonstrated dislocation punching at whisker ends during cooling of the metal-matrix composites [5].

(8) Calculations of dislocation punching distance agree well with the observed dislocation distribution.

3. Experimental method

The composite material selected for this investigation was the same material used in the previously mentioned characterization study [6] and was a 2124 powder metallurgy aluminum alloy containing 13.2 vol.% SiC whiskers. In order to form a basis for comparison, a control alloy with an identical processing history from the same powder batch containing no reinforcement was also studied. The material was received as-extruded, in bars measuring 12.74 mm × 127 mm × 1500 mm in size. The heat treatments were designed to achieve identical values of microhardness in the unreinforced control alloy and in the matrix of the reinforced material. The heat treatment schedules were chosen to obtain two underaged conditions, the peak aged condition, and two overaged conditions as outlined in Table 1. After heat treatment, the samples were stored in a commercial freezer in order to prevent any aging at room temperature.

Tensile tests were performed on an Instron screw-driven testing machine at room temperature using samples conforming to ASTM standard E8-83 for sub-size specimens. The samples were machined prior to heat treatment because machining has been shown to alter the aging state

TABLE 1 All samples solutionized 504 °C for 4h and water quenched

Aging time h at 177 °C		
Condition	Reinforced	Unreinforced
UA1	1	1
UA2	2	4
PA	4	12
OA1	12	16
OA2	16	24

of the material [16]. The strain rate applied to the samples was $2.7 \times 10^{-4} \text{ s}^{-1}$ and strain was monitored with a clip gage type extensometer mounted on the sample. Load and strain output were recorded directly on a HP model 7044A XY recorder for subsequent analysis. Microscopic examination of the fracture surfaces was performed with an AMR model 1000A scanning electron microscope.

4. Finite element formulation and material model

The finite element analysis is based on a convected coordinate Lagrangian formulation of the field equations with the initial unstressed state taken as a reference. All field quantities are considered to be functions of convected coordinates, y^i , which serve as particle labels, and time, t . This formulation has been employed extensively in previous finite element analyses, see, for examples, refs. 17-19.

Attention is confined to quasi-static deformations and, with body forces neglected, the rate form of the principal of virtual work is written as

$$\Delta t \int_V \{ \tau^{ij} \delta E_{ij} + \tau^{ij} u_{,i}^j \delta u_{,i}^j \} dV \\ = \Delta t \int_S \bar{T}^i \delta u_i dS - \left[\int_V \tau^{ij} \delta E_{ij} dV - \int_S T^i \delta u_i dS \right] \quad (1)$$

Here, τ^{ij} are the contravariant components of the Kirchhoff stress: $\tau = J\sigma$, with σ being the Cauchy stress on the deformed convected coordinate net and V and S being the volume and surface, respectively, of the body in the reference configuration; $\partial/\partial t = \partial/\partial t$ at fixed y^i and the second term on the right-hand side represents an equilibrium correction term that is used in the numerical procedure to reduce drift from the

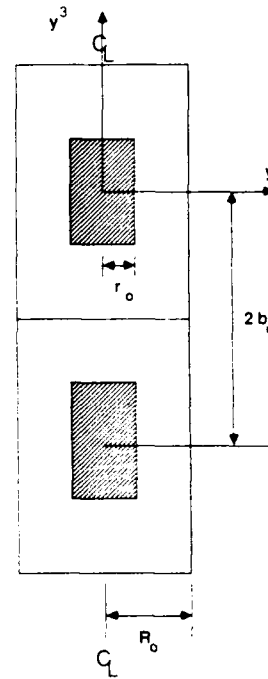


Fig. 2. A schematic diagram of the finite element model. The tensile axis, the y^1 axis, is taken to be the centerline. Because of symmetry conditions, it is only necessary to analyze one quadrant of the unit cell.

equilibrium path due to the discrete time step. The nominal traction components, T^i , and the Lagrangian strain components, E_{ij} , are given by

$$T^i = \tau^{ij} + \tau^{kl} u_{,k}^j v_l \quad (2)$$

$$E_{ij} = \frac{1}{2} (u_{i,j} + u_{j,i} + u_{,i}^k u_{,j}^k) \quad (3)$$

where ν is the surface normal in the reference configuration, u_i are the components of the displacement vector on base vectors in the reference configuration, and $\partial/\partial x_i$ denotes covariant differentiation in the reference frame.

A cylindrical coordinate system (r, θ, z) is used where the identifications $y^1 = r, y^2 = \theta$ and $y^3 = z$ are made. As shown in Fig. 2, we consider circular cylindrical fibers of radius r_0 embedded in a circular cylindrical cell of radius R_0 and length $2L_0$ and with an initial spacing of $2b_0$ between fiber centers. Attention is confined to axisymmetric deformations so that all field quantities are independent of θ and within each cell symmetry is assumed about the center line. Furthermore, the circular cylindrical cell surrounding each fiber is required to remain a circular cylinder throughout the deformation history. As discussed by Tvergaard [20], this axisymmetric configuration can be considered an

approximation to a three-dimensional array of hexagonal cylinders.

The boundary conditions for the axisymmetric region analyzed numerically are:

$$\dot{u}^3 = 0 \quad \dot{T}^1 = 0 \quad \text{on } z = 0 \quad (4)$$

$$\dot{u}^3 = \dot{U}_3 = \dot{\epsilon}_x (b_0 + U_3) \quad \dot{T}^1 = 0 \quad \text{on } z = b_0 \quad (5)$$

$$\dot{u}^1 = \dot{U}_1 \quad \dot{T}^3 = 0 \quad \text{on } r = R_0 \quad (6)$$

Here, $\dot{\epsilon}_x$ is a prescribed constant while \dot{U}_1 is determined from the condition that the average lateral traction rate vanishes, i.e.

$$\int_0^{b_0} \dot{T}^1 dz = 0 \quad \text{on } r = R_0. \quad (7)$$

In addition to the boundary conditions (4) to (7), there is the requirement that displacement components vanish on the surface of the rigid fiber.

In some calculations, a second set of boundary conditions was employed consisting of (4) and (5), but with (6) and (7) replaced by $\dot{T}^1 = 0$ on $r = R_0$, so that every point along $r = R_0$ is stress free. Under these conditions the outer sidewall of the cell does not remain straight and vertical. Of course, for the entire tension specimen, $\dot{T}^1 = 0$ on the outer boundary of the specimen. However, when, as here, the fibers are much smaller than the specimen, the condition that the circular cylindrical cell remain a circular cylinder comes from enforcing geometric compatibility (within the axisymmetric approximation) for a uniform array of fibers perfectly aligned with the tensile axis. Relaxing the boundary condition (6) and (7) permits, in a highly approximate manner, consequences of deviations from this highly constrained fiber distribution to be explored. In subsequent discussion, predictions based on (6) and (7) are referred to as results "with constraint" and predictions based on $\dot{T}^1 = 0$ on $r = R_0$ are referred to as results "without constraint".

The material is characterized as an isotropically hardening elastic viscoplastic solid and the total rate of deformation, \mathbf{D} , is written as the sum of an elastic part, \mathbf{D}^e , and a plastic part, \mathbf{D}^p , with

$$\mathbf{D}^e = \frac{1+\nu}{E} \dot{\boldsymbol{\tau}} - \frac{\nu}{E} (\dot{\boldsymbol{\tau}} : \mathbf{I}) \mathbf{I} \quad (8)$$

$$\mathbf{D}^p = \frac{3\dot{\epsilon}}{2\dot{\sigma}} \dot{\boldsymbol{\tau}} \quad (9)$$

where $\dot{\boldsymbol{\tau}}$ is the Jaumann rate of Kirchhoff stress, \mathbf{I} is the identity tensor, $\mathbf{A} : \mathbf{B}$ denotes $A^i B_i$, $\dot{\epsilon}$ is the

effective strain rate, E is the Young's modulus, ν is Poisson's ratio and

$$\dot{\boldsymbol{\tau}} = \dot{\boldsymbol{\tau}} - \frac{1}{2} (\dot{\boldsymbol{\tau}} : \mathbf{I}) \mathbf{I} \quad \dot{\sigma}^2 = \frac{3}{2} \dot{\boldsymbol{\tau}} : \dot{\boldsymbol{\tau}} \quad (10)$$

$$\dot{\epsilon} = \dot{\epsilon}_0 [\dot{\sigma} / g(\dot{\epsilon})]^{1/m} \quad g(\dot{\epsilon}) = \sigma_0 \dot{\epsilon} / \dot{\epsilon}_0 + 1)^N$$

$$\epsilon_0 = \sigma_0 / E \quad (11)$$

Here, $\dot{\epsilon} = \int \dot{\epsilon} dt$ and the function $g(\dot{\epsilon})$ represents the effective stress vs. effective strain response in a tensile test carried out at a strain rate such that $\dot{\epsilon} = \dot{\epsilon}_0$. Also, σ_0 is a reference strength and N and m are the strain hardening exponent and strain rate hardening exponent, respectively.

Combining eqns. (8) and (9) and inverting gives,

$$\dot{\boldsymbol{\tau}} = \frac{E}{1+\nu} \left[\mathbf{D} + \frac{\nu}{1-2\nu} \mathbf{I} (\mathbf{I} : \mathbf{D}) \right] - \frac{3\dot{\epsilon}}{2\dot{\sigma}} \dot{\boldsymbol{\tau}} \quad (12)$$

For use in eqn. (1), standard kinematic relations are used to express eqn. (12) as a relation between the contravariant components (on the current base vectors) of the convected rate of Kirchhoff stress, $\dot{\boldsymbol{\tau}}''$, and Lagrangian strain rate, \dot{E}_{ij} .

The deformation history is calculated in a linear incremental manner and, in order to increase the stable time step, the rate tangent modulus method of Peirce *et al.* [21] is used. This is a forward gradient method based on an estimate of the plastic strain rate in the interval between t and $t + \Delta t$. The incremental boundary value problem is solved using a combined finite element Rayleigh-Ritz method, Tvergaard [19].

5. Experimental results

Representative stress-strain curves for the unreinforced control alloy and the reinforced composite material are shown in Fig. 3. The addition of the whiskers causes an increase in the elastic modulus, 0.2% offset yield strength and ultimate strength, and a decrease in the strain to failure for the composite material. These effects are well documented in the literature [1-5, 9, 10]. What is more surprising, however, are the effects of aging state on the stress-strain behavior of the composite material. Though the aging curve for the unreinforced control alloy (variation of 0.2% offset yield strength as a function of aging time exhibits the well known "bell-shaped" curve, the composite yield strength is independent of aging time (Fig. 4(a)). The ultimate strength of the

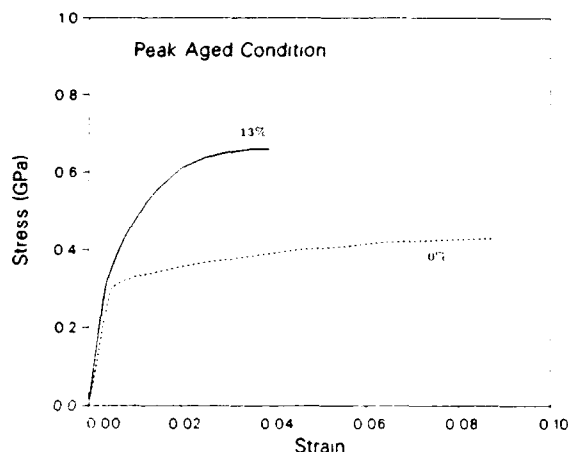


Fig. 3. Representative stress-strain curves for the composite material labelled 13% and the unreinforced control alloy labelled 0%. The increase in the Young's modulus, yield strength, and ultimate strength and decrease in the ductility for the composite material should be noted.

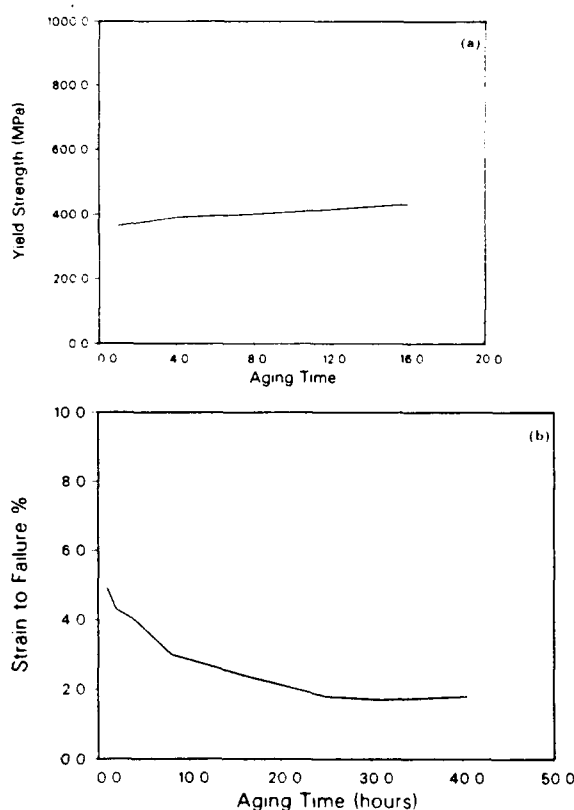


Fig. 4. The variation of a) the yield strength and b) the ductility with aging time.

composite (about 650 MPa) is also independent of aging time. However, the strain-to-failure of the composite is a strong function of aging time, decreasing monotonically from about 5% in the

as-quenched condition to about 1.5% in the severely overaged microstructure, Fig. 4(b).

Microscopic examination of the fracture surfaces revealed a dimpled fracture surface for both the reinforced and unreinforced materials. The fracture surface of the unreinforced material contained a rather even distribution of large dimples connected by sheets of smaller dimples indicating a pattern resulting from ductile void growth, coalescence and failure, Fig. 5. The fracture surface of the reinforced material contained only small dimples similar to the small dimples on the fracture surface of the unreinforced material, Fig. 6(a). The aging time had no detectable effect on the appearance of the fracture surface. Whisker pullout was sometimes observed; although, the pulled-out whiskers were coated with matrix material, Fig. 6(b). This demonstrates that the failure of the composite was predominantly through the matrix and not along the matrix-reinforcement interface. Similar conclusions were also obtained in the fracture studies on SiC whisker and particulate reinforced 2XXX and 7XXX alloys [22].

6. Observations of void formation at elevated temperatures

One mechanism that appears to contribute to the unusually low ductility of Al-SiC whisker composites involves the formation of voids at fiber ends. Nutt and Duva [23] have observed voids forming at room temperature in a 6061 alloy reinforced with SiC whiskers strained to various amounts. Nutt and Needleman [24] have developed a quantitative description of the void nucleation process at fiber ends and compared the predicted and observed modes of failure initiation. While further studies are needed to establish the link between void formation at whisker ends and overall failure mechanisms at room temperature, our recent work indicates that cavitation at whisker ends plays a greater role in controlling the overall constitutive response of Al-SiC composites at elevated temperatures than at room temperature.

The initiation of voids at whisker ends was studied in the same 2124-SiC whisker-reinforced composite described earlier. When the test temperature is increased, the tensile ductility of the Al-SiC composites increases significantly [25]. We have explored this temperature-dependent phenomenon through TEM observations of spec-

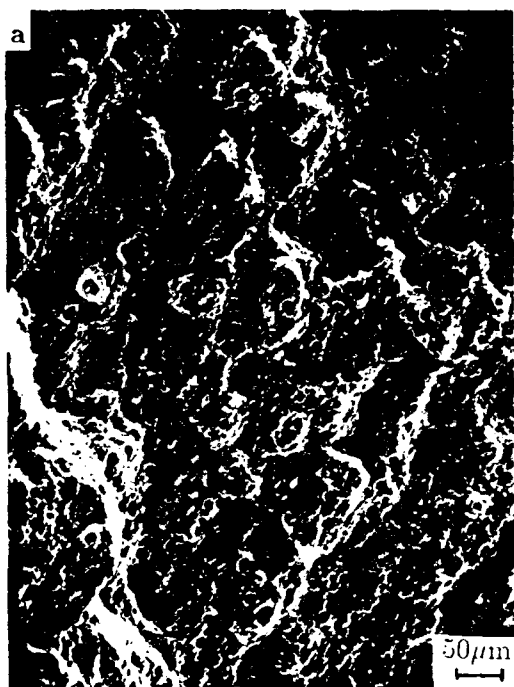


Fig. 5. Fracture surface morphology of the unreinforced control alloy: a—showing the distribution of the large dimples and b—showing the distribution of the small dimples.

imens tested in tension at 300°C. In these experiments, we have used the specimens in the naturally aged condition, as the specimens tested at 300°C quickly achieve a severely overaged matrix microstructure. After the tensile tests,



Fig. 6. Fracture surface morphology of the composite material. The composite shown in Fig. 5 b, should be noted. A pulled-out fiber coated with matrix material is shown in b.

IFM specimens were sectioned from tensile specimens that had undergone different amounts of plastic strain. Voids were typically observed at fiber ends in specimens with macroscopic plastic

strains ranging from 3% to 12.5%. The voids generally formed at the corner on the fiber end, as shown in Fig. 7(a), and intense plastic deformation occurred in the vicinity of the fiber end, as evidenced by the high dislocation density in that region. Glide of the dislocations was inhibited by the coarse age-hardening precipitates that grew

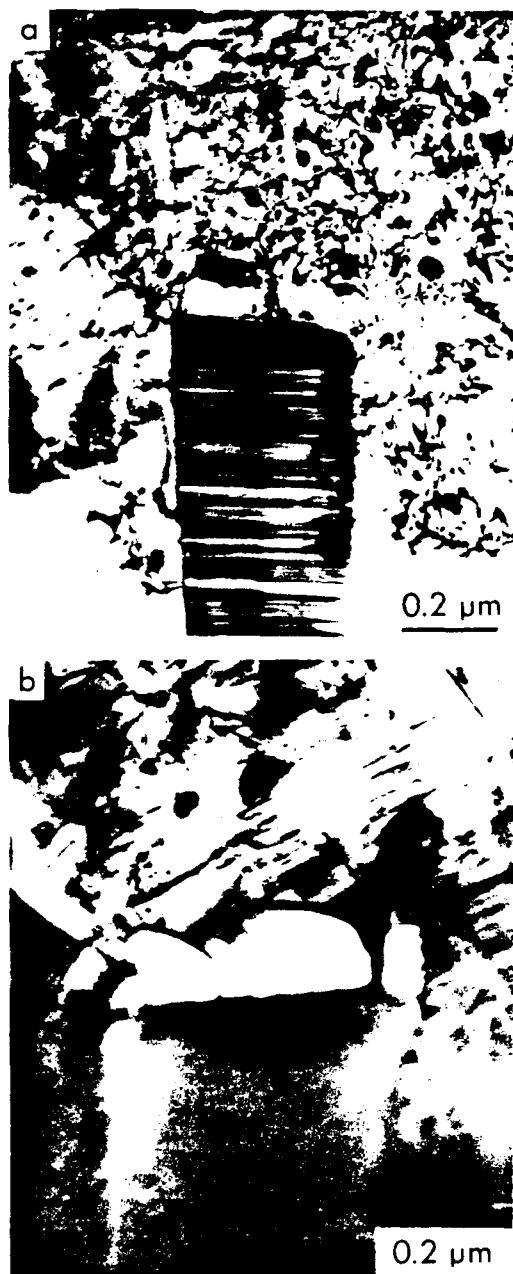


Fig. 7. Void nucleation at fiber ends in 2124 Al-SiC whisker composite deformed at 300 °C to a tensile strain of 0.12. a. Void at corner of fiber end surrounded by dislocated matrix. b. Coalescence of voids formed at different sites on the fiber end.

during the high temperature test, although the high local stresses still produced large plastic strains in this region. With increasing strain, additional voids formed at other corner sites of the same fiber end (Fig. 7(b)), and eventually the voids coalesced to form one large void equal in width to the fiber diameter.

After macroscopic tensile strains of 12.5%, elongated cavities were often observed at fiber ends, as shown in Fig. 8(a). The salient features of the cavitation mechanism are: (1) the cavity width does not exceed the fiber diameter, (2) there is no apparent separation along the fiber side, and (3) the tip of the cavity has retained the same basic shape displayed by much smaller cavities associated with lower strain levels. Furthermore, similar elongated cavities were observed at fiber breaks, as shown in Fig. 8(b). These observations indicate that large amounts of shearing at or near the interface can occur after decohesion at the fiber end, and that the load-bearing capacity of the fibers can be severely reduced.

Patterns of void evolution observed in 2124 Al-SiC composites tested at 300 °C resemble the observations from room-temperature tests in other composite systems in that voids nucleate near the corners of fiber ends and subsequently coalesce to form a single void. However, the distribution of voids differs in that voids nucleate throughout the gage length during the high-temperature tests, while in room-temperature tests the voids are confined to regions very near the fracture surface. Thus, one effect of temperature is to allow the damage to accumulate in the composite microstructure prior to failure, thereby increasing the ductility. These observations suggest that one path to improving the room-temperature ductility of Al-SiC composites would be to identify microstructural parameters that could control the development of cavitation. Toward this end, calculations based on an interface decohesion model are being carried out to determine the effects of microstructural parameters on void formation.

7. Discussion

The results of the tensile tests conducted in this study are useful for the evaluation of composite strengthening theories. The Modified Shear Lag Model [26] predicts the yield strength of the composite material using a model based on simple transfer of shear across the whisker-matrix inter-

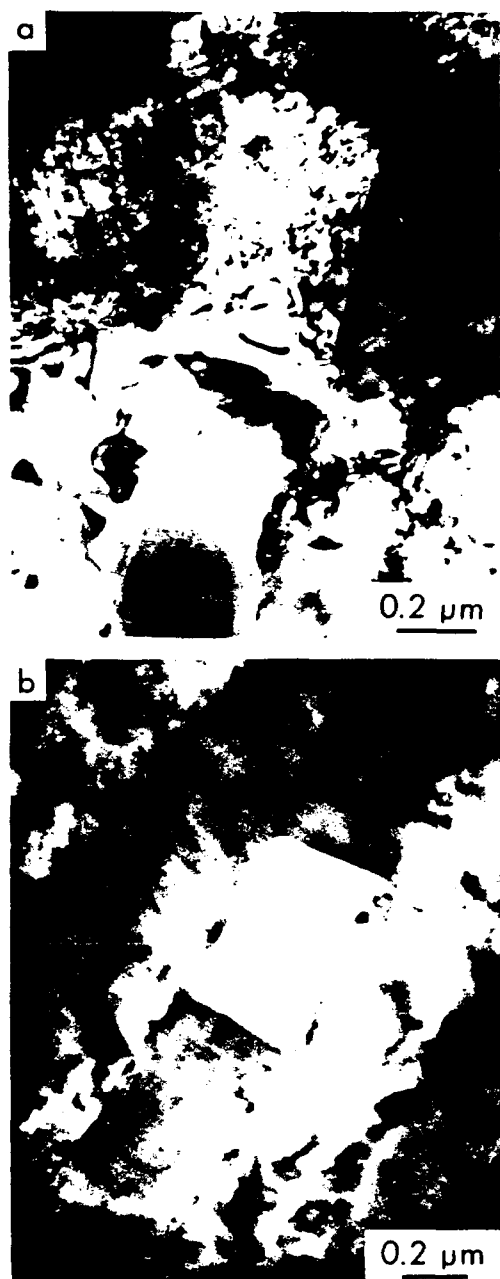


Fig. 8. Void growth in 2124 Al-SiC whisker composite deformed in tension at 300°C. (a) Elongated cavity at the fiber end surrounded by dislocations. (b) Cylindrical cavity at the fiber break.

face with an additional term used to account for load transfer across the ends of the whiskers. This theory, as well as the widely known rule of mixtures theory, are not in qualitative agreement with the experimental observations as they would also predict that the yield strength of the composite material would increase with an increase in

the yield strength of the matrix. The Enhanced Dislocation Density Model [27] attempts to predict the yield strength of discontinuously reinforced metal-matrix composites based on a modified shear lag model taking into account the differences in dislocation densities between the reinforced and unreinforced materials. The qualitative predictions of this theory, however, are in contradiction with the experimental observations of the present study. If the yield strength of the matrix of the composite is significantly different from that of the unreinforced alloy, then one would expect to see this difference reflected as a uniform increase in the microhardness values for the matrix of the composite material. Figure 1a indicates that the matrix of the composite material has about the same hardness as the unreinforced alloy. Also, this theory would predict that the yield strength of the composite material will mirror that of the unreinforced alloy as a function of aging time, although this is not observed experimentally. Thus the Enhanced Dislocation Density Model is not in qualitative agreement with the experimental results and therefore is of questionable value for identifying the strengthening mechanisms for the present material.

In ref. 28 a self-consistent formulation for the hardening behavior of discontinuously reinforced metal-matrix composites was developed, in an attempt to predict the yield strength and hardening exponent. The analysis in ref. 28 is based on a path independent deformation theory of plasticity and depends on the use of Ilyushin's theorem [29]. In this formulation the hardening exponents of the reinforced and unreinforced materials are identical. This is contradictory to the present experimental observation that there is a difference of about a factor of three between the hardening exponent of the reinforced and unreinforced materials. In view of the lack of an adequate, analytically tractable model for the yield and hardening behavior of materials reinforced with discontinuous fibers, a finite element method was used in this study.

The finite element method possesses several inherent advantages over many of the more analytical methods. First, geometrical effects, such as corners at fiber ends, can be handled in a straightforward manner. The simplification required in many theoretical developments of reducing the inclusion from a cylinder to an ellipsoid is not necessary. Second, the calculation of stress and strain contours within the matrix and at the

matrix-reinforcement interface are possible. Third, complete stress-strain responses, as opposed to certain portions of the stress-strain curves, are predicted. Therefore, a finite element approach is appealing for this application. Here, an axisymmetric finite element unit cell model is employed where the aspect ratio of the whisker is the average aspect ratio observed experimentally and the aspect ratio of the unit cell is taken to be approximately equal to the whisker aspect ratio. A similar finite element model, but using a full three-dimensional cell geometry, is described in ref. 30.

The finite element method predictions for uniaxial loading are qualitatively in agreement with the experimental results. Figure 9(a) shows the predicted stress-strain curves as a function of the volume fraction of reinforcement for whisker-reinforced 2124 Al in an underaged state. The effects of matrix aging condition on the stress-strain response are plotted in Fig. 9(b).

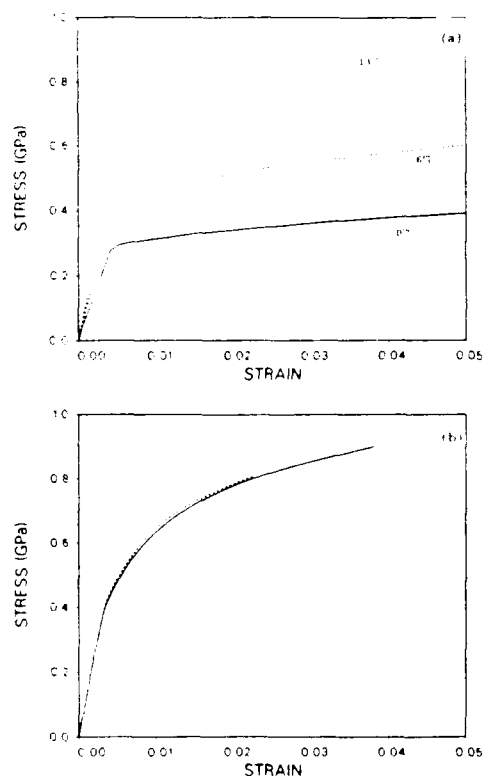


Fig. 9. Qualitative response of the finite element model. a. Finite element predictions as a function of volume per cent of the reinforcement phase. b. Finite element predictions as a function of matrix aging condition; the dashed line is for the peak-aged microstructure and the solid line is for an underaged condition.

The finite element model correctly predicts that the yield strength of the composite material is independent of matrix variations due to aging and that the strain-hardening exponent of the composite be quite different from that of the unreinforced material.

The quantitative predictions for stress-strain response, however, are not within acceptable bounds of the experimental results. Figure 10 shows the predicted and experimental stress-strain curves for an underaged condition in the composite material. The calculated curves, with a traction-free lateral side and with the sidewall constraint representing the periodic array imposed, bound the experimental results, although, they are not sufficiently close to be of use.

The analysis of the effects of the sidewall constraint on the response of the unit cell is useful in attempting to understand the underlying strengthening mechanism for these materials. Without the imposed constraint, there is little increase in the yield strength of the composite over that of the unreinforced control alloy. The increase in yield strength of these materials appears to originate not from direct load transfer to the reinforcement phase but from the constraint of geometrical compatibility.

The distribution of hydrostatic stress within the unit cell, with and without the sidewall constraint, elucidates this mechanism further for identical geometries and aging states at similar values of far-field axial strain, Fig. 11. The differ-

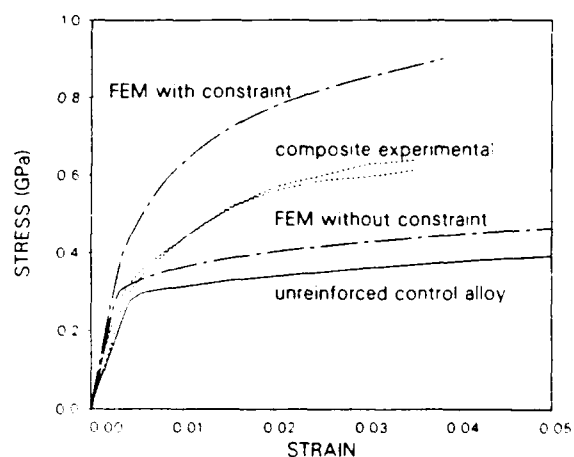


Fig. 10. Comparison of the finite element predictions with and without the sidewall constraint with the experimental results. The finite element predictions bound the experimental results but are too far apart to be of quantitative value.

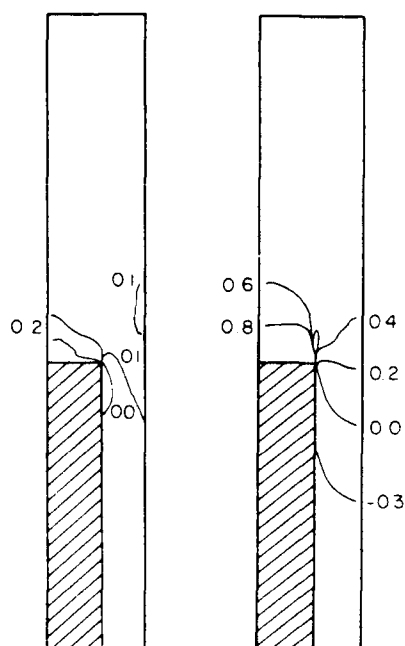


Fig. 11. Distribution of hydrostatic stress in GPa within the unit cell, with and without the sidewall constraint. The values of far field axial strain is almost identical in both cases. The shaded portion of the figure represents the whisker.

ence in far-field axial stress is about 300 MPa, which is approximately equal to the difference in the values for hydrostatic stress within the upper region of the cell. As far-field strain accumulates, the sidewall in the upper portion of the cell attempts to contract at a greater rate than in the lower portion of the cell. The sidewall constraint forces the lateral side to remain straight, thereby generating large compressive hydrostatic stresses within the lower portion of the cell and large tensile hydrostatic stresses within the upper portion of the cell. It is these tensile hydrostatic stresses which appear to increase the yield strength of the composite material rather than direct load transfer to the reinforcement phase.

The cell model, "with constraint", *i.e.* based on the boundary conditions (6) and (7), represents an ideal regular array of perfectly aligned fibers and appears to overpredict the levels of hydrostatic stress generated within the material. In certain regions of the cell, the tensile hydrostatic stress component reaches three times the yield strength of the matrix material. At the present time, it is not clear that such high levels of hydrostatic tension are actually achieved and there are a variety of mechanisms that could act to reduce the hydrostatic tension. For example, deviations

from the aligned end-to-end fiber geometry assumed in the calculations would be expected to lead to reductions in the hydrostatic tension levels achieved. Indeed, preliminary analysis of this effect by the authors indicate significant reductions are so attained.

In the calculations discussed so far the fiber has been taken to be rigid. A few calculations were carried out accounting for fiber elasticity. In these calculations Young's modulus for the SiC fibers was taken to be 450 GPa and Poisson's ratio, $\nu = 0.17$ [31]. Compared with the rigid fiber analysis, there is a reduction in the Young's modulus of the composite of 8%–10%. Also, the peak hydrostatic tension is reduced by 5%–10% when fiber elasticity is accounted for. These calculations show the quantitative magnitude of effects associated with fiber elasticity and indicate that in the Al-SiC system investigated there is no qualitative difference in behavior arising from the assumption of rigid fibers.

The present finite element model makes no attempt to predict ductility. However, the predictions, in conjunction with the experimental results, provide some insight into possible failure modes at room temperature. The failure of the composite appears to be strongly dependent on the matrix material. Recent work by Christman and Suresh [32] on the response of the composite material and control alloy to fatigue loading demonstrated that under these conditions the behavior of the composite is controlled by the failure of the matrix material. The lack of exposed whiskers on the fracture surface and the strong dependence of the ductility on aging raise questions as to the relative roles of voids at the whisker-matrix interface and those within the matrix of the composite.

The large amounts of local deformation observed on the fracture surface in the form of dimples suggests that a void formation mechanism is present. This is consistent with the high levels of hydrostatic stress predicted by the finite element model. Even though the existence of the high levels of hydrostatic tension predicted by the finite element model is uncertain, the existence of significant tensile hydrostatic stresses within the matrix material appears plausible. The generation of these localized tensile hydrostatic stresses, in the matrix slightly above the whisker, may be a driving force for void formation in the matrix material at relatively low values of far-field axial strain.

It should be stated that other metal-matrix composite materials in other studies have displayed strikingly different fractographic features and failure modes [33, 34]. The dependence of ductility on reinforcement chemistry and morphology, matrix chemistry and processing techniques is evident, although not well documented or characterized. The need for systematic studies of the dependence of ductility in metal-matrix composite systems on these parameters is clear. A basis for such a study should be a thorough investigation of ductility in a single metal-matrix composite system.

8. Concluding remarks

In this study, the uniaxial tensile stress-strain response of a 2124 Al-SiC whisker metal-matrix composite was investigated as a function of controlled matrix microstructural variations. The 0.2% offset yield strength of the composite material was independent of aging time despite a significant change in the yield strength of the unreinforced control alloy. Several models available in the literature for composite strengthening were reviewed and discussed in relation to the experimental results of this study and an earlier microstructural characterization study [6]. A finite element unit cell model was shown to predict the correct qualitative trends, although good quantitative accuracy was lacking. The results of the finite element model were discussed in an attempt to develop a better understanding of the strengthening mechanisms in these materials.

The mechanisms involved in the tensile quasi-static failure of the metal-matrix composite were investigated at room temperature and at 300 °C. Void formation mechanisms appeared to play a dominant role in the failure behavior at both temperatures. Although the precise role of the voids in the fracture process remains unclear at this time, voids nucleating at whisker ends appear to be more predominant at elevated temperatures than at room temperature. Further investigation is required to determine the dominant characteristics of voids formed at the whisker-matrix interface and those formed within the matrix of the composite. In addition, the mechanisms influencing the strong dependence of ductility on aging condition remain to be demonstrated.

Acknowledgments

The work of T. Christman and S. Suresh was supported by National Science Foundation Grant NSF-ENG-8451092. Support for A. Needleman and S. Nutt was provided by the Office of Naval Research through contracts N00014-86-K-0261 and N00014-86-K-0125. The authors also gratefully acknowledge the use of Brown University Materials Research Group Central Facilities, funded by the National Science Foundation.

References

1. H. J. Rack and J. W. Mullins, in *High Strength Powder Metallurgy Aluminum Alloys*, The Metallurgy Society of AIME, Warrendale, PA, 1985, p. 155.
2. T. G. Nieh and R. E. Karlak, *J. Mater. Sci. Lett.*, **2**, 1983, 119.
3. M. D. Skibo, *SANL Rep. SAND81-8212*, 1981, Sandia National Laboratories, 1981.
4. D. L. McDaniels, *Metall. Trans. A*, **16**, 1985, 1105.
5. G. Mott and P. K. Liaw, *Rep. 86-7D4-MAX-11*, 1986, Westinghouse R&D Center.
6. T. Christman and S. Suresh, *Acta Metall.*, **36**, 1988, 1691.
7. I. Dutta and D. L. Bourell, to be published.
8. T. G. Nieh and R. E. Karlak, *Sci. Metall.*, **18**, 1984, 25.
9. W. A. Logsdon and P. K. Liaw, *Eng. Fracture Mech.*, **24**, 1986, 737.
10. A. P. Divecha, S. G. Fishman and S. D. Karmarkar, *J. Met.*, **33**, 1981, 12.
11. R. N. Wilson and P. G. Partridge, *Acta Metall.*, **13**, 1965, 1321.
12. G. C. Weatherly and R. B. Nicholson, *Philos. Mag.*, **17**, 1968, 801.
13. D. J. Thompson, *Metall. Trans. A*, **6**, 1975, 671.
14. M. Taya and T. Mori, *Acta Metall.*, **35**, 1987, 155.
15. M. Vogelsang, R. J. Arsenault and R. M. Fisher, *Metall. Trans. A*, **17**, 1986, 379.
16. T. Christman and S. Suresh, unpublished results, Brown University, Providence, 1987.
17. A. Needleman, *J. Mech. Phys. Solids*, **20**, 1972, 111.
18. A. Needleman, in E. H. Lee and R. L. Mallet, eds., *Plasticity of Metals at Finite Strain, Theory, Computation, and Experiment*, Rensselaer Polytechnic Institute, Troy, NY, 1982, p. 387.
19. V. Ivergaard, *J. Mech. Phys. Solids*, **24**, 1976, 291.
20. V. Ivergaard, *Int. J. Fracture*, **18**, 1982, 237.
21. D. Peirce, C. F. Shih and A. Needleman, *Computers Struct.*, **18**, 1984, 875.
22. D. L. Davidson, *SRI Rep. N00014-85-C-0206*, 1987, Southwest Research Institute.
23. S. R. Nutt and J. M. Duva, *Sci. Metall.*, **20**, 1986, 1055.
24. S. R. Nutt and A. Needleman, *Sci. Metall.*, **21**, 1987, 705.
25. V. C. Nardone and J. R. Strife, *Metall. Trans. A*, **18**, 1987, 109.
26. V. C. Nardone and K. M. Prewé, *Sci. Metall.*, **20**, 1986, 43.

- 27 R. J. Arsenault, *Mater. Sci. Eng.*, **64**, 1984, 171.
- 28 J. M. Duva, *J. Eng. Mater. Tech.*, **106**, 1984, 317.
- 29 A. A. Ilyushin, *Prikl. Mat. Mekh.*, **10**, 1946, 347.
- 30 J. M. Papazian and A. Levy, *Symp. on Interfacial Phenomena in Composites*, Newport RI, June, 1988.
- 31 C.-H. Andersson and R. Warren, *Composites*, **15**, 1984, 16.
- 32 T. Christman and S. Suresh, *Mater. Sci. Eng.*, **A16**(2), 1988, 211-216.
- 33 C. P. You, A. W. Thompson and I. M. Bernstein, *Sci. Metall.*, **21**, 1987, 181.
- 34 J. J. Lewandowski, C. Liu and W. H. Hunt, Jr., in *Powder Metallurgy Composites*, The Metallurgical Society of AIME, Warrendale PA, in press.

An analysis of the effect of residual stresses on deformation and damage mechanisms in Al-SiC composites

G. L. Povirk, A. Needleman and S. R. Nutt

Division of Engineering, Brown University, Providence, RI 02912 (U.S.A.)

(Received April 6, 1990)

Abstract

The effect of thermally induced residual stresses on the mechanical properties and ductility of Al-SiC composites was investigated numerically. The predicted behavior in uniaxial loading was calculated with and without the inclusion of the residual stresses which result from the mismatch in thermal expansion between aluminum and SiC. In this analysis, void nucleation by interfacial debonding at the whiskers' ends was assumed to be the limiting failure mechanism. Two cases, both with a fiber volume fraction of 20% and fiber aspect ratio of 4, but with different fiber spacings, were considered. The residual stresses had a small effect on the predicted ductility of the composite, even when a relatively weak interface strength was assumed. The residual stresses are shown to redistribute as interfacial failure is approached. A close end-to-end fiber spacing gives a greater flow strength in compression than in tension and the residual stresses which arise during thermomechanical processing tend to enhance this effect.

1. Introduction

Aluminum alloys reinforced with silicon carbide whiskers display significant increases in stiffness, tensile strength, and creep resistance when compared with unreinforced alloys [1-3]. Unfortunately, the composites also exhibit poor ductility, which has thus far limited their application as a structural material. A better understanding of the underlying mechanisms affecting composite properties is therefore essential if the material is to be improved.

Transmission electron microscopy (TEM) observations by Nutt and Duva [4] revealed that void nucleation at the whisker ends occurred near the surface of fractured specimens. The decohesion of the matrix from the whisker end at low macroscopic strains appears to contribute to the poor ductility observed in Al-SiC composites. Other damage mechanisms observed experimentally include void nucleation by fiber breakage [5, 6] and void growth and coalescence in the matrix itself [5, 7].

Nutt and Needleman [8] analyzed Al-SiC composites within the framework of interface debonding developed by Needleman [9]. Further calculations [10] predicted a transition in the

mode of debonding depending on fiber spacing: debonding initiated at the whisker corner for close side-to-side spacings of fibers but began in the fiber center when spacings were close end-to-end. Examination of a fractured Al-SiC specimen [6, 8] using TEM tended to confirm the results, as debonding in the whisker center was generally only observed when fiber spacing was close end-to-end. The strong similarities of observed and predicted patterns of void evolution suggested that it may be possible to quantify interface properties by comparing experimental observations and predictions based on finite element calculations. However, the calculations in refs. 8 and 10 assumed that the composite was initially stress free.

Arsenault and Taya [11] observed yield strengths higher in compression than in tension for a 6061 aluminum alloy reinforced with SiC whiskers. In addition, they modeled the matrix as a bilinear solid and used Eshelby's solution [12] for an ellipsoidal inclusion to arrive at estimates of residual stresses and the resulting effect on uniaxial stress-strain behavior. Similar experiments and analyses have also been performed by Warner and Stobbs [13]. The limitations of applying Eshelby's solution to Al-SiC composites

include assuming temperature independent material properties and ellipsoidal whiskers. Approaching the problem computationally allows the incorporation of more realistic matrix constitutive behavior and fiber geometries.

Residual stresses are inherent in Al-SiC composites owing to the mismatch in thermal expansion between aluminum and silicon carbide. The stresses develop upon cooling after thermomechanical processing of the material. In previous work [14], we investigated the effects of composite microstructural parameters, such as fiber volume fraction, aspect ratio, and spacing, on the resulting residual stresses. In many cases, significant compressive stresses were calculated at the whisker end. Finite element residual stress computations have also been performed by Zywiec and Parks [15] for continuous fiber-reinforced graphite-aluminum composites. The objective of the present work is to examine the effects of the thermally induced residual stresses on mechanical properties and failure of Al-SiC whisker composites by comparing the predicted response when residual stresses are included with the response when the material is initially stress free.

2. Problem formulation

The approach used here is to model the material as a periodic array of hexagonal cylinders, each consisting of an aluminum alloy with an SiC whisker embedded in the center. The hexagonal cylinder can then be approximated as a circular cylinder, so that the problem is then rendered axisymmetric (see Fig. 1). In addition, because of the symmetry, only one quadrant in the r - z plane need be analyzed.

The analysis can be thought of as occurring in two distinct steps. First, a temperature history simulating a quench of the composite is applied to the unit cell depicted in Fig. 1. The cell walls are required to remain straight during the thermally induced deformation, which maintains compatibility with surrounding cells. Additionally, the average stresses along the walls were fixed at zero, simulating the condition that the macroscopic stresses during quenching are zero. Once the residual stress state in the composite has been determined, the mechanical response of the composite subject to uniaxial tension or compression along the fiber axis is simulated. The boundary conditions on the cell walls are that they remain

straight during loading and that the average stresses on the side cell wall vanish. The boundary conditions in both cases are applied by use of a mixed finite element and Rayleigh-Ritz method developed by Tvergaard [16]. The mechanical response of the composite with residual stresses is then compared with the response of the material that is initially stress free.

The fiber-matrix interface is incorporated into the finite element equations by the method presented by Needleman [9]. We note that although the approach is purely continuum, the finite element formulation of the field equations fully accounts for matrix plasticity, thermal expansion, general temperature dependence of material properties, and finite geometry changes.

Completing the finite element equations requires specifying constitutive relations for whisker, matrix and interface. The SiC whiskers are taken to be elastic and the aluminum matrix is modeled as an isotropically hardening elastic-viscoplastic solid. The uniaxial plastic response of the aluminum matrix is given by

$$\sigma = \sigma_0 \left(\frac{\dot{\epsilon}^p}{\dot{\epsilon}_0} \right)^m \left(\frac{\epsilon^p}{\epsilon_0} + 1 \right)^n \quad (1)$$

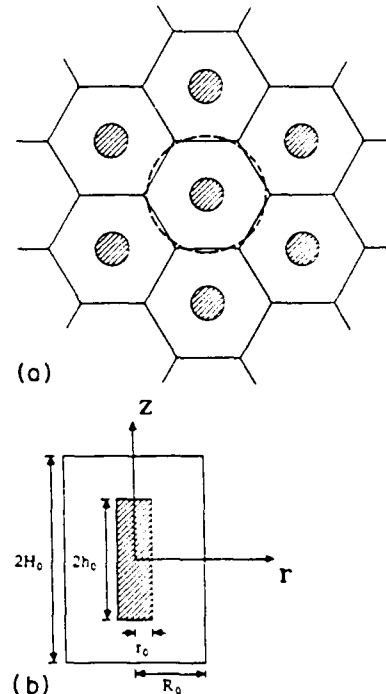


Fig. 1 Schematic diagram showing uniform distribution of whiskers and the geometrical parameters for a single cell. a Cross-section of the composite in the axial direction showing a periodic array of hexagonal cylinders, the dashed line depicts the approximation of a hexagonal cylinder by a circular cylinder. b Side view of a circular cylinder.

The properties of the matrix were chosen to be representative of 6061 aluminum and are given by a reference strain rate of $\dot{\epsilon}_0 = 0.002 \text{ s}^{-1}$, a reference strain of $\epsilon_0 = 0.004$, a strain rate hardening exponent of $m = 0.004$, Poisson's ratio of $\nu = 0.3$, and a coefficient of thermal expansion of $\alpha = 24 \times 10^{-6} \text{ K}^{-1}$. The reference strength σ_0 , strain hardening exponent N , and Young's modulus E were considered to be functions of temperature. Using material data at various temperatures [17], the properties are interpolated by the use of cubic splines. The data specified above result in uniaxial stress-strain curves at various temperatures shown in Fig. 2 in ref. 14. The constitutive relation is generalized to multi-axial states by the usual procedure of replacing the stress and plastic strain appearing in eqn. (1) with their respective von Mises equivalents. A complete development of the constitutive description is given in ref. 14. The property values of β SiC are given by $E = 470 \text{ GPa}$, $\nu = 0.19$, and $\alpha = 4.7 \times 10^{-6} \text{ K}^{-1}$ [18].

A potential ϕ is assumed to exist for the interface, which is taken to depend only on the jump in displacements across the fiber-matrix interface. From the potential, the interfacial tractions (force per unit initial area) are specified by

$$\begin{aligned} T_n &= -\frac{\partial \phi}{\partial u_n} = -\frac{27}{4} \sigma_{\max} \left\{ \left(\frac{u_n}{\delta} \right) \left[1 - 2 \left(\frac{u_n}{\delta} \right) + \left(\frac{u_n}{\delta} \right)^2 \right] \right. \\ &\quad \left. + \gamma \left(\frac{u_t}{\delta} \right) \left[\left(\frac{u_t}{\delta} \right) - 1 \right] \right\} \\ T_t &= -\frac{\partial \phi}{\partial u_t} \\ &= -\frac{27}{4} \sigma_{\max} \left\{ \gamma \left(\frac{u_t}{\delta} \right) \left[1 - 2 \left(\frac{u_n}{\delta} \right) + \left(\frac{u_n}{\delta} \right)^2 \right] \right\} \end{aligned} \quad (2)$$

for $u_n < \delta$, and $T_n = T_t = 0$ for $u_n > \delta$, where u_n and u_t represent the normal and tangential difference in displacements across the interface respectively. As the interface separates, the magnitude of the nominal tractions increases, reaches a maximum, and finally falls to zero when complete decohesion occurs. From eqn. (2) the work of separation ϕ_{sep} at $u_t = 0$ is given by

$$\phi_{\text{sep}} = \frac{9\sigma_{\max}\delta}{16} \quad (3)$$

The interface can thus be characterized by the

strength σ_{\max} , the work of separation ϕ_{sep} , and the shear parameter γ , so that the value of δ is given through eqn. (3). The parameter δ is a phenomenological parameter which characterizes the ductility of the separation, and has dimensions of length.

In the cases studied here, the interface was characterized by $\sigma_{\max} = 3\sigma_0$, where σ_0 is the room temperature yield strength of aluminum, $\delta = 0.005 \text{ } \mu\text{m}$, and $\gamma = 1.0$. Based on TEM observations of voids and calculations performed in ref. 8, the value of the interface strength used here probably represents a weak Al-SiC interface. Comparisons of the most commonly observed void shapes and nucleation sites in ref. 8 suggest that interface strengths of $5\sigma_0$ – $6\sigma_0$ are more likely for aluminum bonded to SiC. Low values for interface strengths were used in the analysis to highlight the effect of residual stresses and because material damage is likely to initiate at poorly bonded interfaces.

3. Numerical results

In computing the residual stresses, the material was taken to be stress free at a uniform temperature of T_0 . A temperature history of the form $T(t) = T_0 \exp(-3.75t)$ (with t in seconds) was applied uniformly over the entire cylinder. Such a history is representative of the temperatures experienced by the material when undergoing a quench in ice water. The spatial uniformity of temperature in the unit cell is justified by calculations in ref. 14, which showed that for realistic quenching rates, plastic deformation in the matrix is unlikely to induce localized heating. Calculations were performed with initial temperatures of either $T_0 = 350^\circ\text{C}$ or $T_0 = 500^\circ\text{C}$, although material properties were held constant beyond 350°C due to lack of available data. The dependence of the resulting residual stresses on the assumed temperature of the initial stress-free state was found to be small. This is anticipated because of the low flow strength of aluminum at high temperatures. The residual stresses used in examining the mechanical behavior of the composite were calculated assuming the material was quenched from $T_0 = 350^\circ\text{C}$.

One result of the study in ref. 14 was that the residual stresses at the whisker end were found to depend primarily on the side-to-side spacing of the fibers. In this investigation, two different spacings of the fibers, henceforth referred to as

cases (a) and (b), were considered, both with a fiber aspect ratio of 4 and a fiber volume fraction of 20%. Case (a) has a cell aspect ratio of 4, giving a ratio of fiber radius to cell radius of $r_0/R_0 = 0.585$, while case (b) was given a cell aspect ratio of 2, yielding a ratio of fiber radius to cell radius of $r_0/R_0 = 0.463$. Decreasing r_0/R_0 corresponds to increasing the side-to-side spacing of fibers and to decreasing the end-to-end spacing of fibers. The calculated average compressive residual stress at the whisker end for case (a) was 175 MPa while case (b) had a value of 401 MPa. It is interesting to note that identical calculations performed with a rigid interface gave average compressive stresses of 176 MPa and 454 MPa for cases (a) and (b) respectively. Apparently, the added compliance of the interface model can affect the predicted results if the residual stresses are high enough. This is particularly true near the fiber corner where very high residual stresses are calculated (around 750 MPa for case (b) with a rigid interface).

3.1. Interfacial decohesion

Figure 2 shows the unit cell stress vs. strain response of case (a), the case with the closer side-to-side fiber spacing, with and without the initial residual stresses included in the analysis. One can interpret the curves as the predicted macroscopic stress vs. strain response of a composite if

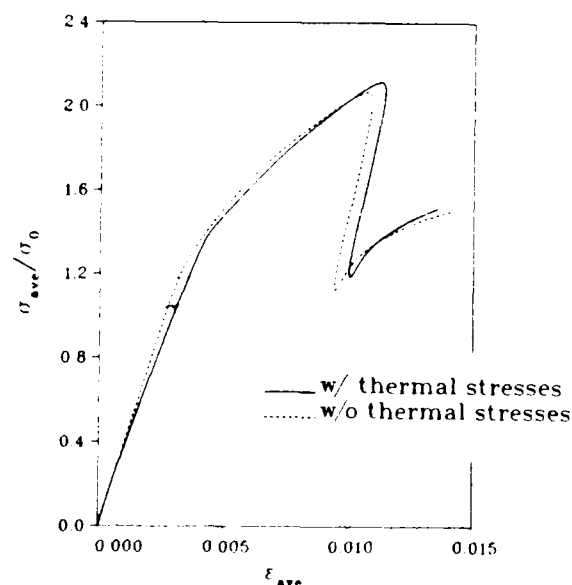


Fig. 2. Stress vs. strain response for case (a), the case with a fiber aspect ratio of 4, a cell aspect ratio of 4 and a fiber volume fraction of 20% (closer side-to-side spacing), with and without residual stresses included.

debonding from every whisker end occurred simultaneously. The maximum stress point on the curves corresponds approximately to the point at which void nucleation begins. In the actual material, one could imagine damage propagating through the composite by initial debonding at a specific whisker, followed by load transfer to surrounding regions and nucleation of new voids. In Fig. 2, the residual stresses have little effect on either the average strain to debonding or the average stress at which debonding initiates.

Figure 3 displays contours of axial stresses near the maximum load point for case (a) with the residual stresses included and with the composite initially stress free. The two stress states are nearly identical, implying that the thermally induced residual stresses are almost completely redistributed by the time the composite reaches maximum load. To further illustrate this, Fig. 4 plots the average normal stress at the fiber end vs. the average applied stress. Given the magnitude of the initial residual stresses, the predicted insensitivity of the overall response to the presence of residual stresses is somewhat surprising. Figure 4 shows that the difference in interface normal stress decreases as the applied load increases, and becomes insignificant near the point of maximum applied stress. The deformed finite element mesh for case (a) at an average strain of $\epsilon_{avg} = 0.0323$ is shown in Fig. 5.

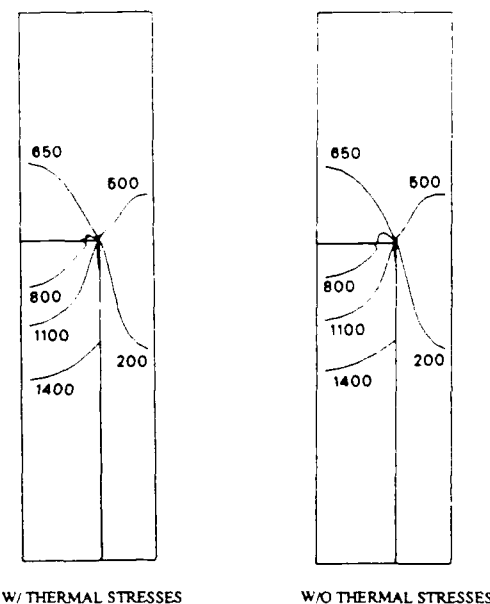


Fig. 3. Axial stresses for case (a), the case with closer side-to-side spacing, near maximum load $\sigma_{avg}/\sigma_0 = 2.0$, with initial residual stresses and with the composite initially stress free.

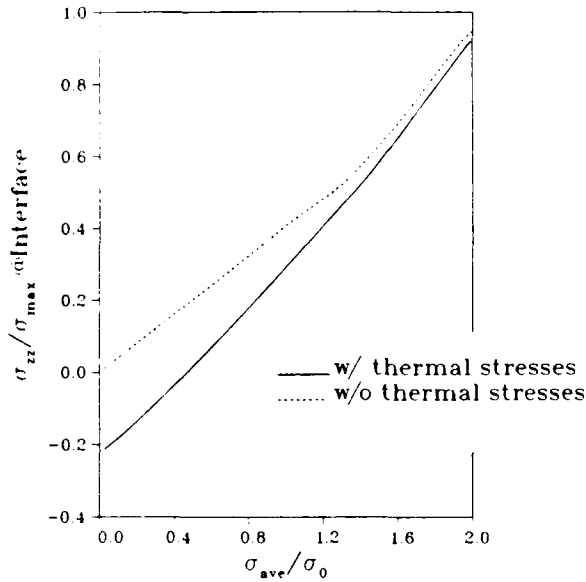


Fig. 4. Average stresses at the interface vs. average applied stress for case (a), the case with closer side-to-side spacing.

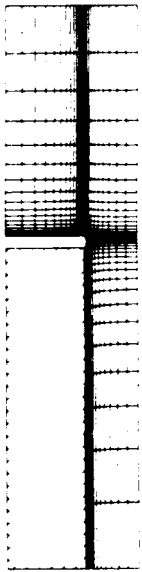


Fig. 5. Deformed mesh for case (a), the case with closer side-to-side spacing, at an average strain of $\epsilon_{ave} = 0.0323$ showing complete debonding at the whisker end.

The calculated stress vs. strain response for case (b), the case with the closer end-to-end fiber spacing, with and without residual stresses included is shown in Fig. 6. Here the residual stresses have a somewhat greater effect on the predicted mechanical response of the composite. Although the stress at which debonding occurs is largely unaffected by residual stresses, a small increase in the strain to debonding is observed.

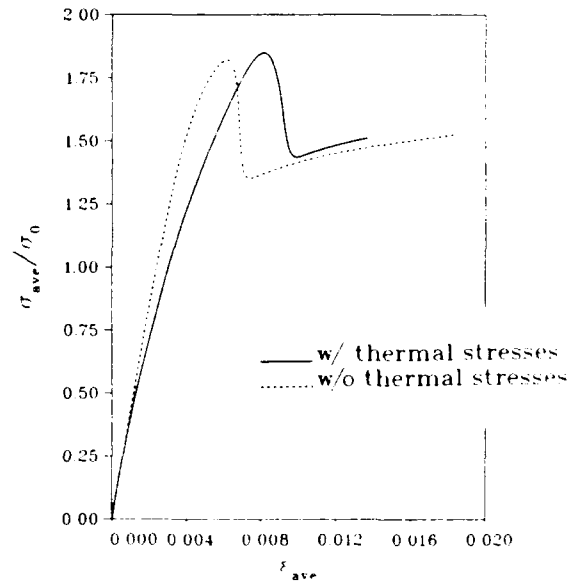


Fig. 6. Stress vs. strain response for case (b), the case with a fiber aspect ratio of 4, a cell aspect ratio of 2 and a fiber volume fraction of 20% (closer end-to-end spacing), with and without residual stresses included.

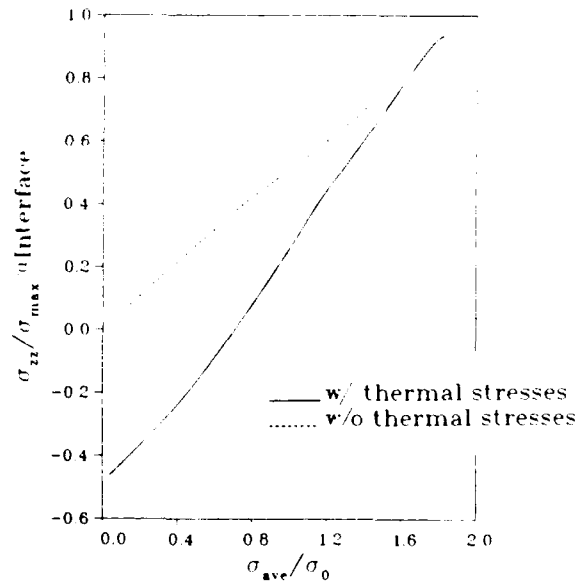
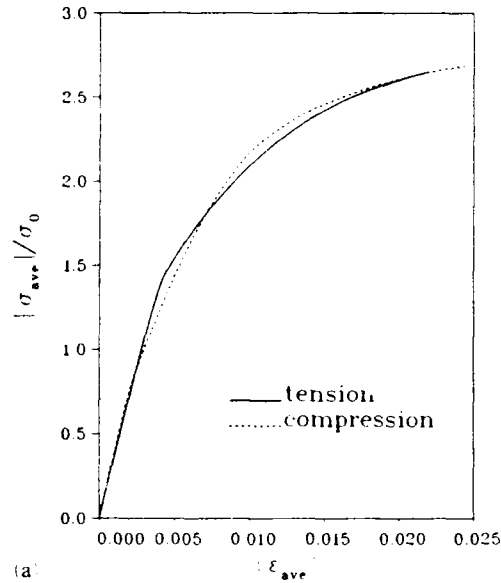
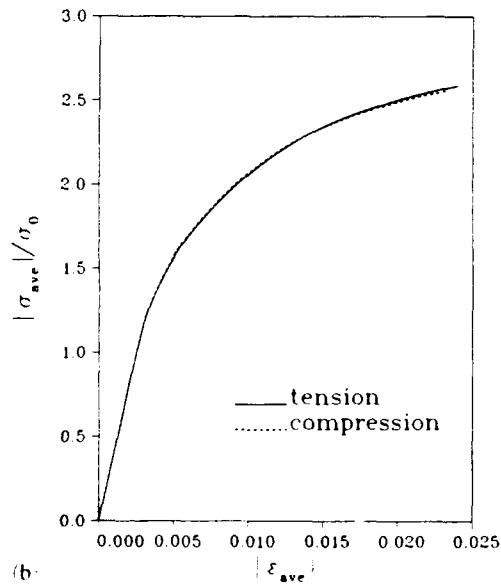


Fig. 7. Average stresses at the interface vs. average applied stress for case (b), the case with closer end-to-end spacing.

Given that the magnitude of residual stresses at the interface is much higher in case (b) than in case (a), a greater effect was expected. Figure 7 displays the average stresses at the interface vs. the average applied stress. Again, as with case (a), as the average stress on the unit cell approaches a maximum, the difference in interface stresses becomes minimal.

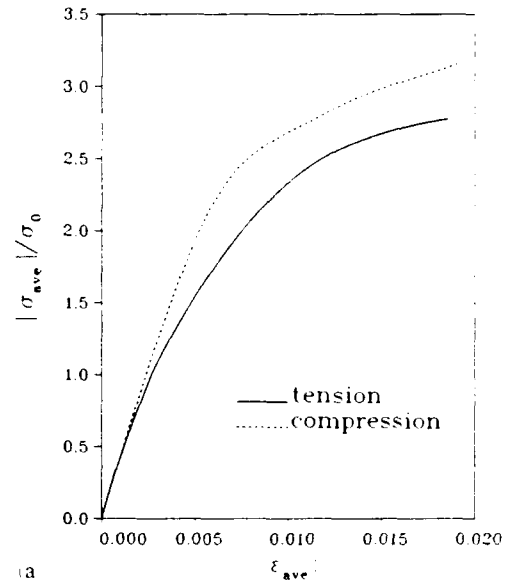


(a)

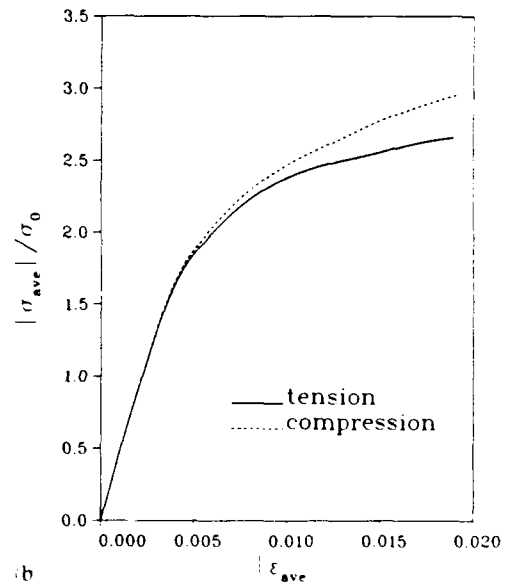


(b)

Fig. 8. Stress vs. strain response in tension and compression for case (a), the case with a cell aspect ratio of 4, closer side-to-side spacing: (a) with residual stresses included, and (b) with the composite initially stress free.



(a)



(b)

Fig. 9. Stress vs. strain response in tension and compression for case (b), the case with a cell aspect ratio of 2, closer end-to-end spacing: (a) with residual stresses included, and (b) with the composite initially stress free.

3.2. Mechanical properties

Figures 8 and 9 show the effect of residual stresses on the uniaxial response in tension and compression. In these calculations, the focus is on the mechanical response of the composite and perfect bonding between fiber and matrix is assumed.

Figures 8(a) and 8(b) respectively, show the uniaxial response in tension and compression of

case (a), the case with the closer side-to-side fiber spacing, with and without residual stresses included in the computations. The unit cell actually yields at a lower stress in compression than in tension for case (a), although by an average strain of 2% the two curves are approaching one another. The reduction of yield strength in compression is not particularly surprising since significant portions of the matrix, most notably near

the fiber corner, have compressive residual stress states. The response in tension and compression is essentially identical for case (a) without residual stresses included.

Figures 9(a) and 9(b) show the computed results for case (b), the case with the closer end-to-end fiber spacing. It should be noted that here the residual stresses have the opposite effect, increasing the yield strength in compression. Also, the yield strengths are asymmetric for case (b), even when no residual stresses are included. Figure 10 shows the large plastic strains that develop between closely spaced fiber ends. This figure illustrates that, at a given level of average strain in compression, there is greater plastic deformation in the matrix between the fiber ends than when the same average strain level is applied in tension. The absolute value of the hydrostatic stress between the fiber ends is also greater in compression than in tension. For close end-to-end fiber spacings, finite geometry change effects, coupled with the constraint of the perfectly bonded fibers on the matrix, result in greater plastic flow between the whisker ends during compressive loading.

4. Conclusions

The effect of thermally induced residual stresses on void nucleation in Al-SiC composites has been investigated by use of the finite element method. The calculations suggest that the residual stresses have only a small effect on either the predicted strength or ductility of the material, at least when ductility is limited by interfacial decohesion. For the material parameters considered here, the residual stresses essentially become fully redistributed as maximum load is approached. It is worth bearing in mind that the cohesive strength used in the calculations probably represents a weak Al-SiC interface. Some calculations were performed with a stronger interface and the residual stresses had an even smaller effect on the predicted ductility of the composite than in the cases shown here. This suggests the possibility that residual stresses may not directly have a significant effect on ductility of materials where the predominant damage mechanism is a plastically deforming matrix separating from hard inclusions (e.g. spheroidized steels, as well as metal matrix composites), although further calculations and experiments

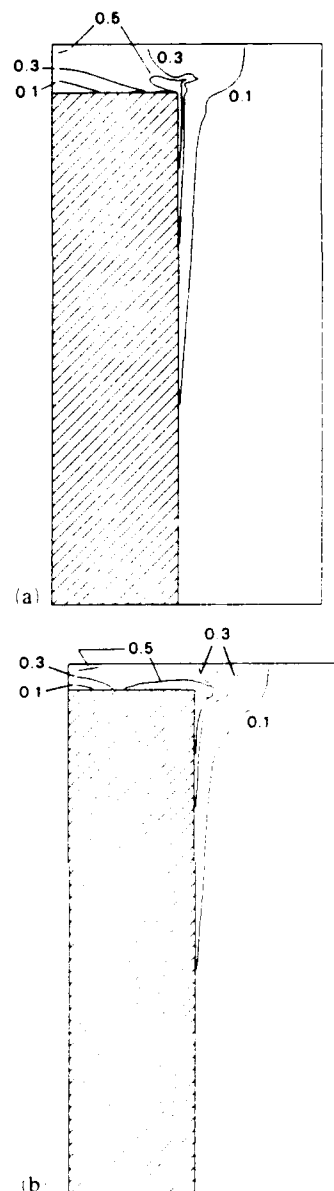


Fig. 10. Effective plastic strain contours for case (b), the case with a cell aspect ratio of 2 (closer end-to-end spacing), and with the material initially stress free: (a) at an average applied strain $\epsilon_{ave} = 0.0273$; (b) at an average applied strain $\epsilon_{ave} = -0.0269$. Note the larger straining between whisker ends in compression.

would be required for confirmation. However, residual stresses can alter the microstructural development of matrix alloys [19], which can in turn affect the ductility of the composite. Furthermore, the residual stresses can still have an important effect on mechanical properties, as illustrated in Fig. 9.

Another important damage mechanism observed in Al-SiC composites is void nucleation

by fiber breakage. Figures 4 and 5 show that the initially large residual compressive axial stresses in the fiber (a calculated maximum of 470 MPa and 980 MPa for cases (a) and (b) respectively) are relieved during tensile loading. While fiber breakage is not incorporated into the present model, the results suggest that whether or not the residual stresses significantly inhibit whisker failure would depend on whether whisker failure occurs before or after the residual stresses are relieved. It should also be noted that there may be a significant effect of residual stresses on deformation and failure mechanisms not considered here.

Comparisons of the mechanical behavior of the composite in compression and tension show that the effect of residual stresses is sensitive to fiber spacing. The initial flow strength in compression was lower than in tension for case (a), the case with the closer side-to-side fiber spacing, although perhaps more importantly, the overall flow behavior in tension and compression was quite similar. In contrast, case (b), the case with the closer end-to-end fiber spacing, showed significantly higher flow strengths in compression. However, it should be recalled that even with (b) taken to be initially stress free, greater flow strengths were predicted in compression than in tension. In fact, Fig. 9 shows that at an applied strain of approximately 2%, the flow strength difference between tension and compression is comparable, with or without residual stresses included in the analysis.

The present results indicate that close end-to-end fiber spacings promote a greater flow strength in compression than in tension. The residual stresses which arise during thermo-mechanical processing tend to enhance this effect. The net contribution of residual stresses to the observed difference between tensile and compressive flow strengths depends on the distribution of fiber spacings.

Acknowledgments

Support from the Office of Naval Research through Contract N00014-86-K-0125 and from the National Science Foundation through Grant MSM-8618007 is gratefully acknowledged. The computations were carried out at the Pittsburgh Supercomputing Center. We are grateful to Professor A. G. Evans of the University of California, Santa Barbara for suggesting the investigation of compressive behavior.

References

1. S. V. Nair, J. K. Tien and R. C. Bates, *Int. Met. Rev.*, **30** (1985) 275.
2. T. G. Nieh, *Metall. Trans. A*, **15** 1984 139.
3. A. P. Dichecha, S. G. Fishman and S. D. Dermarkar, *J. Met.*, **33** 1981 12.
4. S. R. Nutt and J. M. Duva, *Scr. Metall.*, **20** 1986 1055.
5. T. Christman, A. Needleman, S. R. Nutt and S. Suresh, *Mater. Sci. Eng.*, **A107** 1989 49.
6. S. R. Nutt, G. L. Povirk and A. Needleman, unpublished results, 1989.
7. D. L. Davidson, *SRI Rep. N00014-85-C-0206*, 1987 (Southwest Research Institute, San Antonio, TX).
8. S. R. Nutt and A. Needleman, *Scr. Metall.*, **21** 1987 705.
9. A. Needleman, *J. Appl. Mech.*, **54** 1987 525.
10. A. Needleman and S. R. Nutt, in K. Salama, K. Ravichandar, D. Taplin and P. Rama Rao (eds.), *Advances in Fracture Research*, Pergamon, Oxford, 1989, p. 2211.
11. R. J. Arsenault and M. Taya, *Acta Metall.*, **35** 1987 651.
12. J. D. Eshelby, *Proc. R. Soc. London, Ser. A*, **241** 1957 376.
13. T. J. Warner and W. M. Stobbs, *Acta Metall.*, **37** 1989 2873.
14. G. L. Povirk, A. Needleman and S. R. Nutt, *Mater. Sci. Eng.*, **A125** 1990 129.
15. E. Zywicki and D. M. Parks, *Comp. Sci. Tech.*, **33** 1988 295.
16. V. Tvergaard, *J. Mech. Phys. Solids*, **24** 1976 291.
17. *Metals Handbook*, Vol. 2, American Society of Metals, Metals Park, OH, 1979, 9th edn.
18. Battelle Memorial Institute, *Engineering Properties of Selected Ceramic Materials*, American Ceramic Society, Columbus, OH, 1966.
19. T. Christman and S. Suresh, *Acta Metall.*, **6** 1988 1691.

CREEP DAMAGE MECHANISMS IN CERAMIC COMPOSITES

S. R. Nutt and P. Lipetzky

Division of Engineering, Brown University, Providence, RI 02912

Whisker-reinforced ceramics show improvements in a variety of mechanical properties, and because of the inherent thermal and chemical stability of ceramics, it is natural to consider issues related to mechanical behavior at high temperatures. Implementation of ceramic materials in high-temperature structural applications is often limited by creep, and recent studies on $\text{Al}_2\text{O}_3\text{-SiC}_w$ have shown that creep resistance of ceramics can be enhanced by whisker reinforcement. These studies demonstrated that creep response is strongly affected by the presence of the reinforcing phase and the properties of the whisker-matrix interface. In addition, oxidation reactions that occurred during creep degraded interface properties, facilitated microstructural damage, and accelerated creep. The objective of the present study was to determine the effects of test ambients on creep damage mechanisms in $\text{Al}_2\text{O}_3\text{-SiC}_w$ composites and to correlate these observations with compressive creep response under different stress-temperature conditions.

Hot-pressed SiC whisker-reinforced alumina (from Greenleaf Corporation) was selected for the present study. The composite material was characterized by an average grain size of 1-2 microns and a whisker volume fraction of 1/3. The composites were almost completely free of glass phase, at least within the detectability limits of weak beam dark field and phase contrast imaging (Fig. 1). Material was machined into cylindrical samples for compressive creep experiments which were conducted in air and in nitrogen at 1200-1400°C under applied stresses of 25-250 MPa. Creep rates were monitored until a nominal constant strain rate was reached and maintained. Applied loads were incremented for fixed temperatures, although the total accumulated strain was kept below 3%. Creep experiments were interrupted during secondary creep and cooled under load to retain microstructures. Thin foil specimens were sectioned from the center of the samples and prepared by ion milling.

Data from creep experiments performed in nitrogen and in air are summarized in Fig. 2. The effect of the oxidizing ambient was to increase the creep rate by factors of 3-5 for temperatures of 1300-1400°C, respectively. In addition, the stress dependence of the creep rate increased as the temperature increased above 1200°C. The most prevalent damage mechanism observed in all crept samples was void nucleation at grain boundary-interface (GBI) junctions, an example of which is shown in Figure 3. Decohesion occurred after accumulation of aluminosilicate glass at GBI junctions during creep, resulting in glass-lined cavities. In the non-oxidizing ambient, the aluminosilicate phase originated from the small amounts of residual glass films present in the as-fabricated material (Fig. 1), which redistributed during creep. In the presence of air, the amount of glass phase appearing in the composites was increased, a phenomenon attributed to thermal oxidation of SiC near the specimen surface. Silica glass produced by oxidation during creep penetrated the composite along interfaces and grain boundaries, accumulating at GBI junctions and other stress concentrations. An example of the initial stages of thermal oxidation is shown in Figure 4, a phase contrast image of a near-surface SiC whisker after prolonged creep at 1400°C in air. Graphitic carbon and silica glass have formed at the interface, although the carbon subsequently disappears via formation of CO. In all of the crept samples observed, the dislocation density was negligible, leading to the conclusion that the composites had deformed by diffusional creep. However, at creep temperatures above 1200°C, sliding of grain boundaries and interfaces became increasingly unaccommodated, especially in the oxidizing ambient. Glassy films arising from thermal oxidation of SiC weakened internal boundaries in the material, causing extensive microstructural damage (cavitation) and accelerated creep.*

*Work supported by the Office of Naval Research through Contract #N00014-86-K-0125.

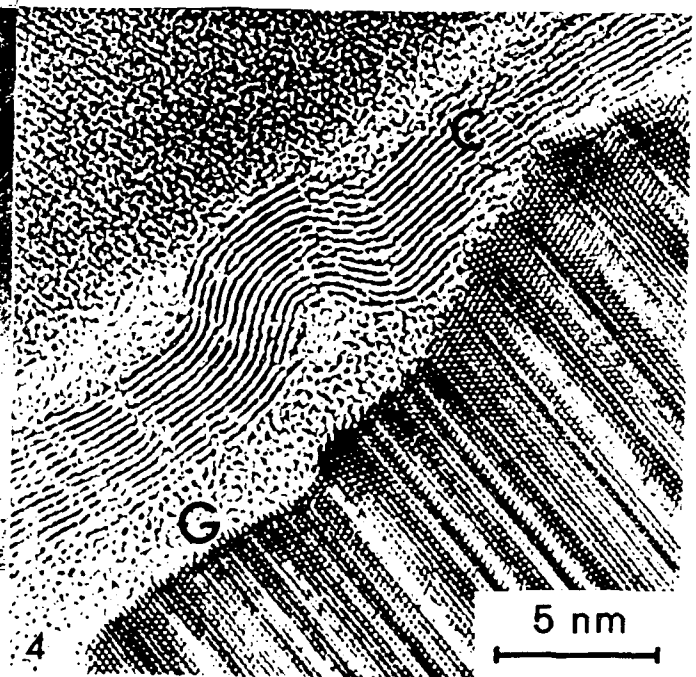
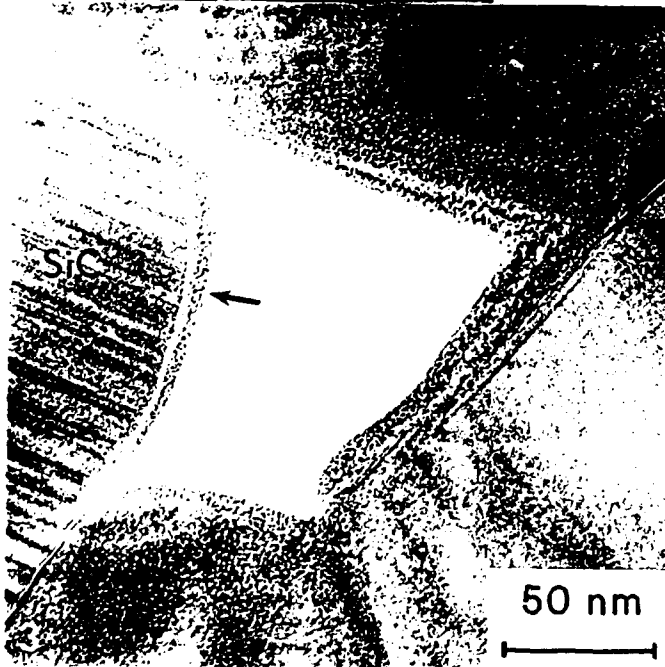
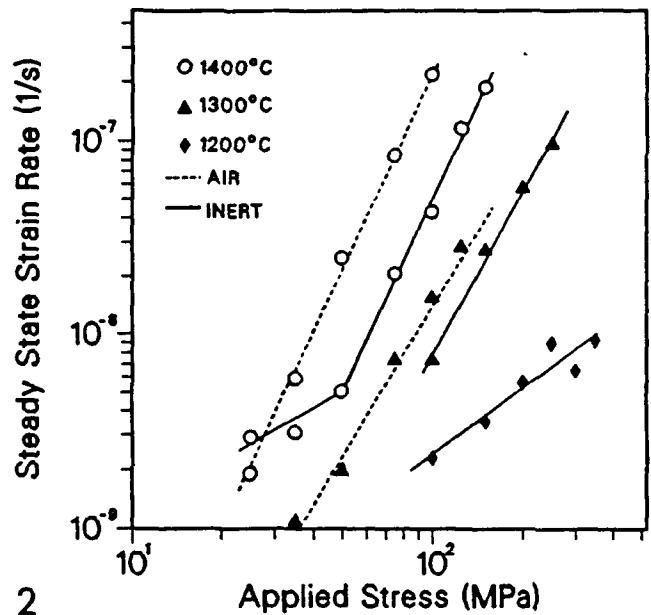
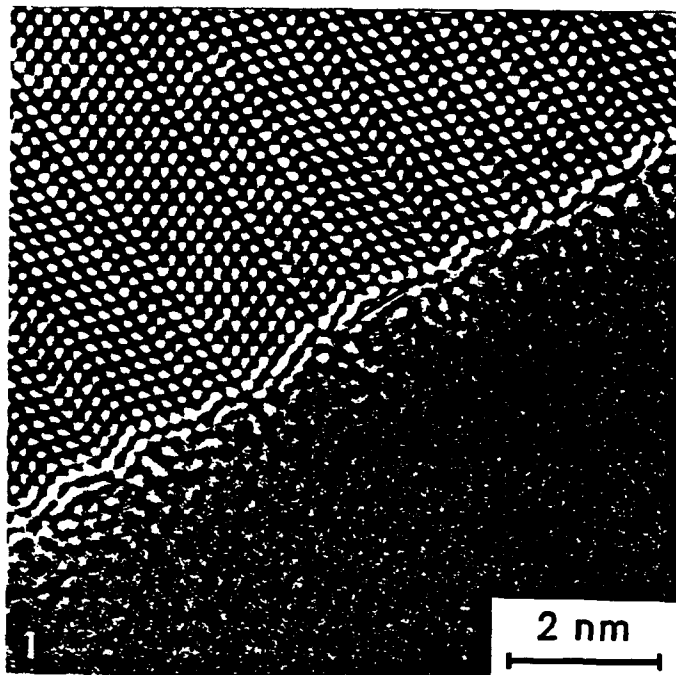


FIG. 1.--Residual glass film, approximately 1 nm thick, at whisker interface in as-fabricated composite.

FIG. 2.--Steady-state strain rates vs. applied stress for creep experiments in nitrogen and in air at 1200-1400°C.

FIG. 3.--Glass-lined cavity at GBI junction resulting from creep in air at 1400°C.

FIG. 4.--Thermal oxidation of near-surface SiC whisker during creep at 1400°C in air, resulting in silica glass (G) and graphitic carbon (C).